Hydrogen Absorption on Single Palladium Nanoparticles

Tingxuan Liu

A thesis
submitted in partial fulfillment of the
requirements for the degree of

Master of Science

University of Washington
2025

Committee:
Bo Zhang
Joshua Vaughan

Program Authorized to Offer Degree:
Chemistry

University of Washington

Abstract

Hydrogen Absorption on Single Palladium Nanoparticles

Tingxuan Liu

Chair of the Supervisory Committee:

Bo Zhang

Department of Chemistry

This study presents a comprehensive investigation into the electrocatalytic behavior of single palladium nanoparticles (Pd NPs) during the hydrogen evolution reaction (HER), with a particular focus on their unique ability to absorb hydrogen into the bulk lattice. Using stochastic single-particle collision experiments at carbon fiber ultramicroelectrodes, we captured and analyzed transient current signals arising from individual NP–electrode interactions under acidic conditions. These current traces revealed distinct kinetic phases associated with hydrogen adsorption (Volmer step), hydrogen evolution (Heyrovsky and Tafel steps), and subsurface hydrogen absorption. Quantitative analysis shows that Pd NPs absorb a significant fraction of the adsorbed hydrogen, leading to reduced HER efficiency compared to bulk Pd electrodes. The observed steady-state and transient currents suggest a strong competition between HER and hydrogen absorption, which alters the effective reaction pathway and suppresses molecular hydrogen formation.

Systematic evaluation of proton concentration and applied overpotential further revealed that the HER kinetics on Pd NPs deviate from classical mechanisms, exhibiting unusually low transfer coefficients and small apparent rate constants. These findings indicate that hydrogen absorption—not hydrogen desorption—is the rate-limiting step under many experimental conditions. By isolating single-particle responses, this work provides critical mechanistic insight into nanoscale hydrogen electrosorption and establishes single-NP collision electrochemistry as a powerful tool for resolving complex catalytic processes involving coupled interfacial and bulk transformations.

Contents

List of Figures

1 Introduction

We present a mechanistic investigation of the hydrogen evolution reaction (HER) and hydrogen absorption on single palladium nanoparticles (Pd NPs) using chronoamperometric collision experiments. By analyzing transient current responses during stochastic NP–electrode interactions, we resolved the sequential processes of proton adsorption, hydrogen evolution, and bulk absorption into Pd. Our results reveal that Pd NPs exhibit pronounced hydrogen absorption, which competes with HER by diverting surface-adsorbed hydrogen into the particle lattice. Compared to bulk Pd, individual Pd NPs show enhanced hydrogen uptake but diminished HER efficiency, particularly under moderate overpotentials. Tafel analysis and kinetic modeling indicate that the HER on Pd NPs deviates from classical Volmer–Heyrovsky or Volmer–Tafel pathways, instead proceeding through a slow, absorption-dominated mechanism characterized by low transfer coefficients and limited catalytic turnover. These findings underscore the role of nanoscale hydrogen absorption in modulating electrocatalytic behavior and highlight the utility of single-NP collision techniques in probing reaction heterogeneity and transport-limited pathways in hydrogen-related catalysis.

1.1 Motivation

The escalating severity of global climate change, driven by greenhouse gas emissions from fossil fuel combustion, has accelerated the shift toward clean, sustainable energy systems.[1] Decarbonizing the energy sector demands scalable alternatives to carbon-intensive fuels, especially for transportation, industry, and grid-scale energy storage. Hydrogen, producible from renewable electricity and emitting only water during use, is a versatile solution with applications in fuel cells, power generation, energy storage, and chemical manufacturing. However, current hydrogen production predominantly relies on fossil fuels, generating more carbon dioxide than the hydrogen offsets (grey or blue hydrogen).[2, 3] This underscores the urgency for green hydrogen production methods, such as electrochemical water splitting, where the hydrogen evolution reaction (HER) at the cathode is critical. The rise of unstable renewable sources like solar and wind energy further highlights the need for energy storage, with water electrolysis offering a practical approach to convert clean electricity into storable hydrogen. Developing efficient, cost-effective HER catalysts is thus essential.

Hydrogen storage remains a significant barrier, with physical methods (high-pressure or cryogenic storage) posing safety risks.[4] Chemical storage using solid-state materials, such as palladium (Pd), offers a safer alternative due to its ability to absorb hydrogen and form hydrides (PdH_x). While Pd has been extensively studied in supported systems—where it is immobilized on substrates like carbon or metal oxides, influencing its catalytic and absorption behavior,[5–12]—the intrinsic electrocatalytic and absorption dynamics of unsupported Pd nanoparticles (NPs), par-

ticularly their interplay under non-equilibrium conditions, remain poorly understood. This knowledge gap, critical for advancing Pd-based hydrogen technologies, motivates our study.

To provide the mechanistic foundation for this investigation, the following section introduces HER, covering its reaction pathways, kinetic models, and mass transport considerations. This overview is essential for understanding how Pd NPs catalyze HER and how hydrogen absorption may influence this process. A brief review of the single NP collision technique employed in this study is also included.

1.2 Hydrogen Evolution Reaction

1.2.1 Acidic HER mechanism

Water splitting process (Equation (1)) involves two processes, the HER on the cathode and the oxygen evolution reaction (OER) on the anode. In different pH environment, the water splitting reaction is composed by different half reactions. In acid, this process contains two reactions as shown in Equation (2) and Equation (3). On the contrary, in alkaline solution, the two half reactions become Equation (4) and Equation (5).

$$\mathrm{H_2O\ (l)} \rightarrow \mathrm{H_2(g)} + \frac{1}{2}\mathrm{O_2(g)} \tag{1}$$

$$2\mathrm{H^+} + 2e^- \rightarrow \mathrm{H_2} \quad (E^\circ = 0.00\ \mathrm{V} \quad \text{vs. SHE}) \tag{2}$$

$$2\mathrm{H_2O} \rightarrow \mathrm{O_2} + 4\mathrm{H^+} + 4e^- \quad (E^\circ = 1.23\ \mathrm{V} \quad \text{vs. SHE}) \tag{3}$$

$$2\mathrm{H_2O} + 2e^- \rightarrow \mathrm{H_2} + 2\mathrm{OH^-} \quad (E^\circ = -0.83\ \mathrm{V} \quad \text{vs. SHE}) \tag{4}$$

$$4\mathrm{OH^-} \rightarrow \mathrm{O_2} + 2\mathrm{H_2O} + 4e^- \quad (E^\circ = 0.40\ \mathrm{V} \quad \text{vs. SHE}) \tag{5}$$

The mechanism of HER under acidic conditions remains incompletely understood, albeit extensively studied.[12–19] In particular, the interaction between protons and electrochemically active surfaces can influence the adsorption behavior and lead to distinct reaction pathways. Noble transition metals, such as platinum (Pt), exhibit unique electrocatalytic characteristics in acid, with Pt being recognized as the most efficient catalyst for water splitting due to its low overpotential requirement and near-zero hydrogen adsorption energy. However, although Pt remains the most efficient catalyst for HER, its high cost and scarcity have motivated the exploration of alternative noble and non-noble metal catalysts. A fundamental understanding of HER mechanisms in acidic conditions is therefore essential for the rational design and optimization of next-generation catalysts.

In acidic media, HER proceeds via the electrochemical reduction of protons, leading to the formation of molecular hydrogen. The reaction follows a two-step mechanism, beginning with the Volmer step (proton adsorption) and followed by either the Heyrovsky step (electrochemical desorption) or the Tafel step (chemical desorption). The reactions are shown in Equation (6) to (8).

$$H^+ + e^- \rightarrow H_{ads} \tag{6}$$

$$H_{ads} + H^+ + e^- \rightarrow H_2 \tag{7}$$

$$2H_{ads} \rightarrow H_2 \tag{8}$$

The rate of the Volmer step is dependent on the hydrogen adsorption free energy (ΔG_{H^*}) of the catalyst. If the adsorption is too weak, insufficient hydrogen will be available for the subsequent steps, whereas if it is too strong, the desorption of hydrogen will be delayed, slowing down the overall reaction. Following the Volmer step, hydrogen gas can be formed through either the Heyrovsky step or the Tafel step. In the Heyrovsky step, an adsorbed hydrogen atom reacts with a proton to form molecular hydrogen. In the Tafel step, two adsorbed hydrogen atoms undergo recombination and form a hydrogen molecule and desorb from the electrode. In fact, these two steps are competing with each other and controlled by many factors, such as kinetics, thermodynamics, mass transfer, and surface coverage.

1.2.2 Mass Transfer in Electrochemical reactions

Many factors affect the HER rate. One of them is mass transfer. In electrochemical systems, it typically involves three fundamental processes: diffusion, migration, and convection. Diffusion refers to the movement of species down their concentration gradients, migration denotes the motion of charged species under an electric field, and convection encompasses the mass transport induced by bulk fluid movement.

In electrochemical experiments involving freely diffusing species, particularly at micro- and nanoscale electrodes, minimizing the contributions of migration and convection is crucial to ensure that the observed signals accurately reflect diffusion-controlled processes. Migration effects are effectively suppressed by the addition of a large excess of inert supporting electrolytes, which screen the electric field and eliminate long-range electrostatic forces. Convection can be minimized by conducting measurements under quiescent, unstirred conditions. Then, mass transport is dominated by diffusion. The diffusion-limited flux of species toward an electrode surface can be described by Fick's first law:

$$J = -D\frac{dC}{dx} \tag{9}$$

where J is the flux (mol cm^{-2} s^{-1}), D is the diffusion coefficient (cm^2 s^{-1}), and dC/dx is the concentration gradient. The steady-state current follows the well-known diffusion-limited expression:

$$i_{ss} = bnFDCr \tag{10}$$

where b is a geometric parameter dependent on the electrode, D is the diffusion coefficient of the reactant, C is the bulk concentration of the reactant and r is the radius of the electrode.

However, at low electrolyte concentrations, suppression of migration becomes less effective. The Debye length λ_D, which characterizes the screening distance of electric fields, increases as the ionic strength decreases:

$$\lambda_D = \sqrt{\frac{\epsilon\epsilon_0 RT}{2F^2 I}} \tag{11}$$

where ϵ is the dielectric constant, ϵ_0 is the permittivity of free space, R is the gas constant, T is the absolute temperature, F is the Faraday constant, and I is the ionic strength. As λ_D increases, electric fields extend further into solution, potentially enhancing migration and electroosmotic flow (EOF), which can affect mass transport and reaction kinetics.

Therefore, while diffusion dominates under high electrolyte conditions, migration and EOF effects must be considered when operating at low ionic strengths, especially in nanoscale systems. This consideration becomes particularly critical when interpreting electrochemical processes involving small entities such as NPs.

1.2.3 HER kinetics

The second factor that can influence HER rate is the kinetics. While the underlying mechanistic steps have been well established, the overall reaction rate and its controlling factors can vary depending on the catalyst surface, reaction environment, and overpotential. Understanding the electrochemical kinetics is therefore crucial for identifying the rate-determining step (RDS) and quantifying the catalytic performance.

Under kinetic control—when mass transfer and surface availability are no longer limiting—the kinetics of an electrochemical reaction can be described by the Butler–Volmer equation:[20]

$$i = i_0 \left[\exp\left(\frac{\alpha nF\eta}{RT}\right) - \exp\left(-\frac{(1-\alpha)nF\eta}{RT}\right) \right] \tag{12}$$

where i is the current density, i_0 is the exchange current density, the current density when $\eta = 0$. α is the transfer

coefficient, n is the number of electrons transferred, η is the overpotential.

The exchange current density i_0 reflects the intrinsic rate of electron transfer at equilibrium and is related to the standard heterogeneous rate constant k^0 by:

$$i_0 = nFAk^0C^* \tag{13}$$

where A is the electrochemically active surface area, and C^* is the bulk concentration of the electroactive species. This relationship provides a bridge between measurable macroscopic current and microscopic electron-transfer kinetics.

At sufficiently high overpotential, one exponential term dominates, but the other one can be canceled, leading to the Tafel approximation:

$$\eta = a + b \log i \tag{14}$$

where a is a constant related to i_0 and b is the Tafel slope, given by:

$$b = \frac{2.303RT}{\alpha nF} \tag{15}$$

The magnitude of the Tafel slope provides mechanistic insights into the HER. Typically, a Tafel slope of approximately 120 mV dec^{-1} suggests that the Volmer step is rate-limiting, while a slope of approximately 40 mV dec^{-1} indicates a Heyrovsky (electrochemical desorption) limited process. A Tafel slope of around 30 mV dec^{-1} is characteristic of a Tafel rate-determining step under ideal conditions.[14]

However, recent studies have revealed that Tafel slope values are influenced by additional factors beyond the identity of the RDS. Microkinetic modeling by Shinagawa et al.[13] showed that a Heyrovsky rate-determining step can also yield a Tafel slope of 120 mV dec^{-1} at high hydrogen surface coverage ($\theta_H > 0.6$), highlighting the need to consider coverage-dependent kinetics. Moreover, van der Heijden et al.[14] emphasized that mass transport limitations, electrolyte concentration, and interfacial effects can distort the observed Tafel slopes, especially under low ionic strength or poor proton supply conditions. They proposed the use of Tafel slope plots to validate the kinetic significance of measured slopes, recommending the identification of horizontal regions where the slope remains constant with respect to current density.

Therefore, systematic Tafel analysis, combined with careful control of mass transport conditions and extraction

of kinetic parameters such as the standard rate constant (k_0) and transfer coefficient (α), is essential for accurately diagnosing HER mechanisms, particularly on complex catalytic systems such as single Pd NPs.

1.2.4 Volcano Plot

In addition to mass transport and interfacial kinetics, the intrinsic catalytic activity of the material also plays a critical role in HER. To understand catalytic efficiency from a kinetic perspective, scientists proposed the Volcano Plot, which typically relates the hydrogen adsorption free energy (ΔG_{H^*}) to the logarithm of the exchange current density ($\log i_0$). As early as 1920, Paul Sabatier proposed the Sabatier principle, which states that the interaction between the catalyst and the reactants should be moderate to achieve the highest catalytic efficiency.[21] Based on this principle, Balandin constructed an early volcano plot for different HER catalysts, while Trasatti later incorporated hydrogen adsorption energy and electrode work function to explain variations in electrocatalytic efficiency.[22, 23] Thus, the best catalyst for HER should have a hydrogen adsorption free energy $\Delta G_{H^*} \approx 0$, meaning that the binding strength of adsorbed hydrogen is thermoneutral with respect to molecular hydrogen in the standard state (1/2 H_2).

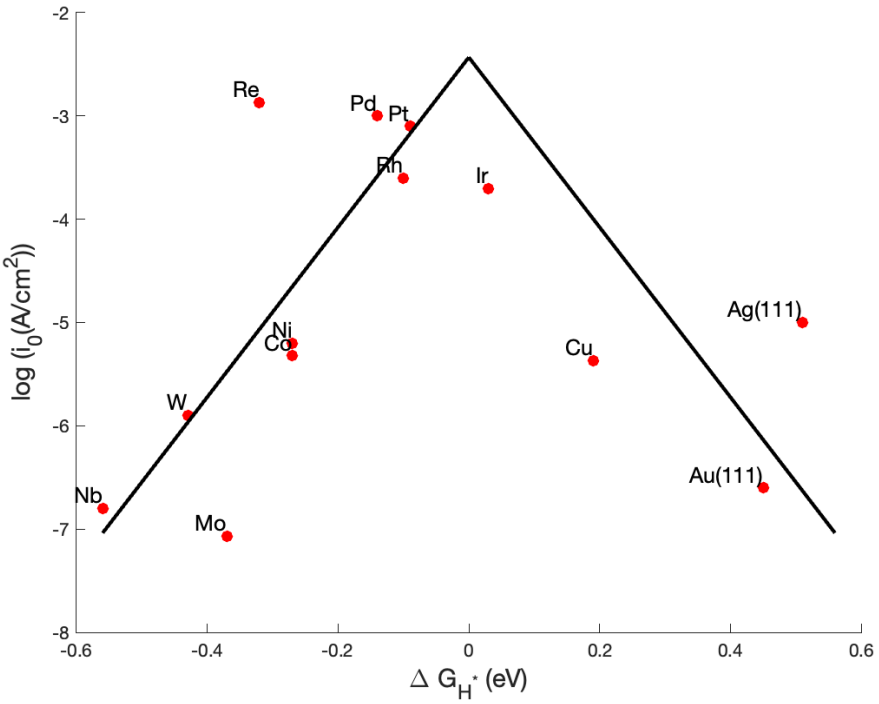

Figure 1: Volcano plot illustrating the relationship between the hydrogen adsorption free energy (ΔG_{H^*}) and the exchange current density ($\log i_0$) for the HER. The data points represent various transition and noble metals, with labels indicating the corresponding materials. A second-order polynomial fit was applied to the data for $\Delta G_{H^*} < 0$, and the resulting curve was symmetrically mirrored about $\Delta G_{H^*} = 0$ to reflect the Sabatier principle. This plot is reproduced based on data from [24].

Subsequent density functional theory (DFT) calculations by Nørskov et al.[24] quantitatively established the volcano relationship for HER catalysts, further confirming that platinum (Pt) sits near the apex with an almost thermoneutral ΔG_{H^*}, while Pd lies slightly off the maximum but still exhibits favorable hydrogen binding energetics. While the Sabatier principle remains a widely used framework for understanding HER catalysis, especially for noble metals near the volcano apex, its application has notable limitations. Quaino et al. [25] highlighted that oxide layers, multi-site adsorption, and kinetic complexities can significantly distort the ideal volcano-shaped relationship between ΔG_{H^*} and HER activity, suggesting that such plots should be interpreted with caution. Nevertheless, since our study focuses on Pd—a transition metal located near the volcano apex—this framework remains solid and is thus adopted here to facilitate mechanistic interpretation.

1.2.5 Hydrogen Evolution and Absorption Behavior of Pd

Among the various HER catalysts, Pd has attracted great amount of attention due to its high catalytic efficiency. As shown in Figure 1, the hydrogen adsorption free energy of Pd is very close to that of platinum (Pt), and Pd also exhibits a relatively large exchange current density during HER catalysis.

Unlike Pt, which only adsorbs hydrogen on its surface to form a near-monolayer coverage of approximately 0.92 [26], Pd uniquely enables hydrogen absorption into its bulk lattice, forming Pd hydrides (PdH_x) and undergoing phase transitions and surface rearrangements during operation [27, 28]. These coupled interfacial and bulk processes can influence HER kinetics and catalytic performance. Yakabe et al. proposed a two-step kinetic model for hydrogen absorption into Pd-based amorphous films, consisting of Langmuir-type surface adsorption followed by bulk penetration, providing a mechanistic framework to understand how interfacial and bulk processes can independently influence hydrogen uptake [6]. Hubkowska et al. systematically demonstrated that thin-film Pd electrodes (Pd-LVE) provide a reliable and versatile model system for studying hydrogen electrosorption across aqueous and non-aqueous electrolytes, offering detailed electrochemical protocols and analytical methods for quantifying adsorption and absorption processes [7]. Schwarzer et al. quantitatively determined the adsorption, absorption, and surface-to-bulk diffusion energetics of hydrogen on Pd surfaces, and proposed that hydrogen absorption significantly competes with desorption and must be considered in Pd-based catalytic systems [8].

Moreover, at the nanoscale, the physical and chemical properties of Pd NPs can differ significantly from those of bulk Pd, due to size-dependent effects on surface structure, electronic properties, and diffusion dynamics [9]. These differences may further impact the hydrogen adsorption, absorption, and catalytic processes at the NP level, potentially leading to behaviors distinct from those observed in bulk materials. Zalineeva et al. demonstrated that octahedral Pd NPs

exhibit significantly enhanced hydrogen absorption capacity (up to $x = 0.90$) and distinct thermodynamic behavior compared to bulk Pd, due to their facet-dependent core–shell–skin structure and nanoscale lattice relaxation [10]. Narayan et al. further revealed, via in situ TEM, that hydrogen phase transformation in single Pd nanocubes proceeds through corner nucleation and front propagation along $\{100\}$ planes, followed by defect self-healing, highlighting the remarkable structural resilience of Pd NPs during repeated absorption cycles [29].

Numerous studies have investigated the HER on loaded Pd NPs supported on substrates such as carbon or metal oxides, revealing high catalytic activity and significant hydrogen absorption effects. For instance, Pd NPs on carbon supports exhibit enhanced HER performance due to optimized hydrogen adsorption energies, with absorption into the Pd lattice influencing reaction kinetics.[10] Similarly, Pd NPs embedded in microporous carbon derived from apricot shell biomass have demonstrated excellent HER performance in alkaline media, with a Tafel slope of ~31 mV/dec and sustained activity over 50 hours.[11] The study emphasizes that optimal NP size (e.g., 5 nm) and appropriate matching with the carbon pore structure are critical for maximizing active site exposure and catalytic efficiency. In another example, Aygün et al. reported that Pd NPs embedded at the step edges inside graphitized nanofibers (PdNP@GNF) exhibit continually increasing HER activity during prolonged electrochemical cycling, eventually surpassing commercial Pt/C catalysts.[12] This unusual self-enhancement behavior was attributed to dynamic restructuring of the Pd–carbon interface, which hardwired the NPs into the conductive matrix and enhanced hydrogen-related charge transport.

However, these investigations are limited to supported systems, where substrate-induced electronic and interfacial effects complicate the interpretation of intrinsic behavior of indivial NPs. In contrast, our study focuses on unsupported, freely dispersed Pd NPs to isolate and probe the intrinsic dynamics of hydrogen evolution and absorption at the single-particle level.

1.3 Previous work on nanoparticle collision

1.3.1 Invention of NP collision

Stochastic single nanoparticle collision is not a novel concept, but one with a history. They were first electrochemically detected in 2004, where inert NPs blocked redox mediator diffusion, resulting in current decreases stepwise.[30] In 2007, Xiao et al. reported single NP collision events involving electrocatalytic reactions.[31] In their experiments, as shown in **Scheme 1a**, electrocatalytically active Pt NPs were added into the acid solution. They diffused freely under Brownian motion and collide with an inert carbon fiber electrode stochastically. In the absence of NPs, no current signal was observed. Upon collision, the NPs catalyzed electrochemical reactions at the electrode–solution interface,

producing various current signals that reflected the electrocatalytic activity and dynamics of individual particles. In their 2008 work, Xiao et al. investigated hydrazine oxidation catalyzed by platinum NPs, and systematically categorized the resulting current responses into two types: staircase signals, which result from NPs adhering to the electrode and generating a steady-state current; and peaks, which arise from transient catalytic events where the NP detaches shortly after collision.[32] This distinction provided important mechanistic insights into NP–electrode interactions and laid the foundation for interpreting signal types in single-entity electrochemistry. Beyond HER and hydrazine oxidation, in 2010, Kwon et al. extended the single NP collision approach to oxidative electrocatalysis, demonstrating the oxygen evolution reaction (OER) at the level of individual IrO_x NPs. When these NPs collided with a relatively inert (for OER) Pt UME held at anodic potentials, transient current spikes were observed, suggesting that the NPs were either blocked from sustained contact or detached rapidly from the electrode surface.[33]

As pioneers, Bard group studied the relation between NP size and the steady-state current. The steady-state current can be estimated by the following equation:

$$i_{ss} = 4\pi \ln(2) nFDCr \tag{16}$$

Here, 4π comes from the spherical geometry of the NPs, and n is the number of electrons transferred during the reaction. F is the Faraday constant and D is the diffusion coefficient of the analyte species. C is the concentration of the analyte, and r is the radii of the NPs. In the equation, the term ln 2 comes from the blockage of diffusion to the NPs by the electrode.[31, 32] In their work, they also recognized that the collision frequency is a function of the electrode surface area, NP concentration, and NP diffusion coefficient.[32] However, a more quantitative relation is given later in 2011 by Kwon et al: [34]

$$f = 4D_{NP}C_{NP}r_{electrode} \tag{17}$$

1.3.2 Development of NP collision

After this, single-entity collision electrochemistry has rapidly evolved into a versatile platform for probing NP behavior at the nanoscale. Early efforts focused on detecting individual collision events and extracting fundamental kinetic parameters. Kahk et al.[35] first demonstrated the extraction of standard electron transfer rates and transfer coefficients from single Ag NP collisions, establishing the feasibility of probing electrochemical kinetics at the single-entity level. Building upon this, Anderson and Zhang[36] systematically correlated immobilized and colliding NPs to structural features, enabling direct structure–function mapping. Pushing the temporal resolution frontier, Defnet et al.[37] employed microjet-assisted collisions to resolve ultrafast hydrogen adsorption and evolution dynamics on

individual Pt NPs under high-acid conditions.

Single-NP collision studies were soon extended beyond basic detection toward mechanistic understanding. Zhou et al. demonstrated size estimation of Ag NPs from anodic current transients during oxidation, and later quantified the particle sticking probability to be around 15 percent.[38, 39] Ortiz-Ledón and Zoski correlated electrochemical events with AFM imaging, confirming that observed collisions correspond to actual NP adsorption events.[40] Robinson et al. revealed that partial electrooxidation of Ag NPs involves multiple stochastic micro-collisions, challenging earlier assumptions of single-impact events.[41] Sun, Wang, and Chen[42] attributed multi-peak collision signals to dynamic variations in electrical contact rather than detachment. McKelvey, Robinson, and White further demonstrated that only about half of the oxidized Ag during NP collisions is recovered as soluble Ag^+, suggesting the concurrent formation of insoluble oxide species.[43]

Surface binding dynamics were systematically studied by Ma et al., who showed that adsorption strength critically influences collision current signatures and developed a collision-based sizing method.[44] Xu et al. applied an AI-assisted multiparameter analysis to classify Ag NP sizes from electrochemical collision signals, enabling higher-resolution size discrimination beyond conventional current-based methods. [45] In hydrogen evolution studies, Xiang et al. revealed that the transformation of current transients from spikes to staircases during Pt NP collisions is governed by interfacial kinetics and catalyst passivation under hydrogen-rich conditions.[17] Hao and Zhang extended collision studies to probe compositional changes, capturing real-time electrochemical dealloying and core–shell oxide formation in Ag–Hg NPs. [46]

To enhance control over collision dynamics, external fields have been introduced. Magnetic fields were used by Santos et al. to guide Fe_3O_4–Prussian Blue NP collisions, and magnetophoretic strategies were developed by Yoo et al. for attomolar-level detection of DNA-linked Ag NPs [47, 48]. Forced convection via stirring or wall-jet flow was shown by Jiang et al. to increase collision frequency, albeit with complex flow-rate dependencies [49]. Light-controlled NP generation and collisions were demonstrated by Wang et al., expanding single-entity studies into photoelectrocatalysis [50].

Beyond metallic systems, Boika et al.[51] detected insulating NPs such as silica and polystyrene spheres via blocking of redox mediator diffusion, particularly under low ionic strength conditions. Optical visualization of collisions has also advanced; Ma et al.[52] developed an electrochemiluminescence (ECL) microscopy platform capable of distinguishing elastic versus adhesive collisions, while Defnet and Zhang[18] used ECL reporting to capture ultrafast HER dynamics at single Pt NPs in real time.

Electrode surface modifications have emerged as a key strategy to regulate collision behavior. Kim et al.[53]

modulated Au NP collision frequency and residence time by tailoring surface monolayer functionalities. Enzymatic strategies were introduced by Castañeda et al.[54] to activate catalytic collisions via exonuclease digestion of DNA shells, and surface charge modulation was leveraged for tunneling-based collision detection through polyelectrolyte multilayers.[55] Collision studies were also extended to semiconductor surfaces by Ahn and Bard, who detected Pt NP impacts on TiO_2-coated n-type Si electrodes.[56] The choice of electrode material has been shown to strongly influence collision signals. Shin et al. demonstrated enhanced Pt NP detection on Pd UMEs via synergistic electrocatalysis, whereas Jung et al. observed only transient peak-type signals from Pt NP collisions on dynamically oxidizing Cu UMEs.[57, 58]

Recently, single-NP collision methods have been increasingly applied to environmental sensing. Karimi et al. utilized single-particle detection to monitor arsenic adsorption and redox transformation on CeO_2 NPs, while Hosseini Narouei et al. extended these techniques to Fe_3O_4 NPs for quantifying arsenic remediation processes.[59, 60] Oladeji et al. employed impact electrochemistry for Pd recovery from dilute solutions, simultaneously achieving in situ fabrication of Pd/carbon black catalysts for hydrogen evolution and Suzuki coupling reactions.[61]

1.3.3 Pd NP collision

Among the various systems studied, Pd Pd NPs have attracted particular attention due to their catalytic properties more recently. Pd NP collision studies have provided critical insights into nanoscale electrocatalysis. The first detection of single Pd NP collisions was reported by Daryanavard and Zare in 2017, using a chronopotentiometric method based on hydrazine oxidation to monitor transient potential shifts. While demonstrating detection feasibility, their approach was limited by gas-phase byproducts affecting signal stability.[62] Park et al. (2018) later introduced a chronoamperometric strategy employing hydrogen peroxide reduction, a gas-free reaction, to observe Pd NP collisions on gold ultramicroelectrodes (Au UMEs). Their method produced staircase-like current responses with minimal decay, enabling quantitative analysis of single-particle electrocatalytic activity.[63] In 2022, Rudakemwa et al. demonstrated that single-Pd NP collisions on Au UMEs exhibit staircase-like current responses due to stronger adhesion and better catalytic preservation compared to Pt, Cu, and Ni electrodes, providing critical insights for electrode material selection in single-entity electrochemical studies.[64]

Chen et al. employed single-particle chronoamperometry to investigate the HER catalyzed by individual Pd NPs through collision events at carbon UME.[65] Their study focused on tracking the transient catalytic responses associated with single-Pd NP impacts and analyzing the temporal evolution of NP catalytic activity during repeated collision events. However, several aspects of their experimental design and data interpretation warrant further refinement. The

attribution of multiple current peaks within a single detection event to repeated interactions of a single NP was made without supporting statistical analysis or time-scale modeling. The explanation relied solely on empirical observations of current peak patterns, without probabilistic justification to exclude the possibility of multiple independent particle impacts within the same event window.

Furthermore, the NP concentrations employed in the study were extremely low (60–180 fM), resulting in theoretically predicted collision frequencies that should be correspondingly low under simple diffusion-controlled conditions. However, the experimentally observed collision frequencies were significantly elevated compared to these theoretical expectations. To account for this discrepancy, the authors qualitatively ascribed the phenomenon to hydrodynamic trapping effects and invoked the concept of NP retrapping by analogy to prior studies on oxygen-evolving electrocatalytic systems.[66] Nevertheless, the catalytic system investigated here, involving the HER on Pd NPs, fundamentally differs from oxygen evolution in that Pd can absorb hydrogen into its lattice, forming PdH_x during the reaction.[26–28, 67] This absorption process alters the nature of gas generation and NP–UME interactions, potentially reducing the likelihood of retrapping phenomena compared to simple oxygen bubble release. Therefore, the application of retrapping mechanisms to interpret the elevated collision frequencies under HER conditions requires additional experimental validation and should not be assumed a priori. These considerations highlight the need for a more rigorous mechanistic investigation of HER dynamics at the single-Pd NP level, particularly under conditions where hydrogen absorption processes may critically alter catalytic behavior.

1.3.4 Our objective

While HER and absorption mechanisms on bulk and ensemble Pd systems have been extensively studied, a fundamental understanding of H absorption at the single-particle level remains incomplete. In bulk Pd electrodes, hydrogen absorption into the lattice, phase transitions, and hydride formation have been recognized as critical factors influencing catalytic behavior. However, when the catalyst size is reduced to the nanoscale, these processes may evolve differently due to finite-size effects, altered hydrogen diffusion dynamics, and enhanced surface-to-volume ratios. Single Pd NP collisions provide a unique opportunity to isolate individual catalytic events, deconvolve adsorption and hydrogen evolution processes, and directly capture transient phenomena that are otherwise averaged out in ensemble measurements. Furthermore, stochastic variations in HER kinetics, hydrogen absorption, and catalyst deactivation pathways can only be fully captured at the single-particle level. Thus, studying HER at individual Pd NPs is essential for both advancing mechanistic understanding and guiding the rational design of next-generation hydrogen evolution catalysts and hydrogen storage material.

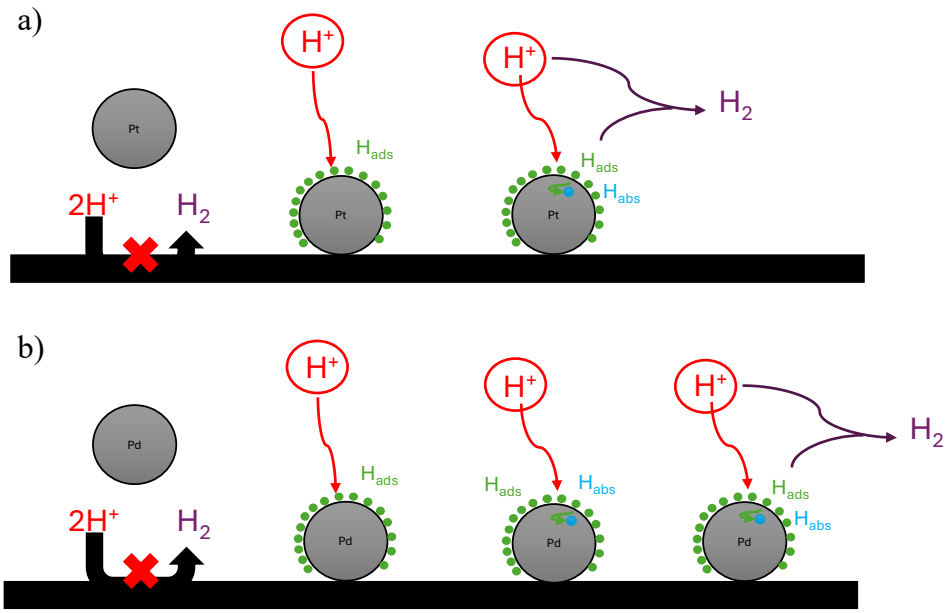

Scheme 1: Schematic illustration of single NP collisions on an inert electrode surface leading to the HER. (a) A Pt NP facilitates HER through surface adsorption and recombination of H_{ads} species. The schemes highlight mechanistic differences in hydrogen handling by Pd and Pt during single-entity electrocatalytic events. (b) A Pd NP collides with the electrode and catalyzes proton reduction, involving sequential adsorption (H_{ads}), absorption (H_{abs}), and H_2 formation.

Here, we present a mechanistic study of hydrogen evolution on individual Pd NPs under acidic conditions and free diffusion. Using chronoamperometric detection of single Pd NP collisions at carbon fiber ultramicroelectrodes (CFUMEs), we systematically investigate hydrogen adsorption, absorption, and electrocatalytic behavior arising from stochastic NP–electrode interactions. By analyzing the evolution of current transients as a function of proton concentration and applied overpotential, we disentangle the Volmer, Heyrovsky, and Tafel contributions to the overall HER process. Notably, our findings reveal significant hydrogen absorption into the Pd lattice during collisions, fundamentally altering the HER mechanism compared to traditional surface-catalyzed systems. In particular, we observe that hydrogen absorption competes with hydrogen evolution, suggesting potential shifts in the rate-determining step. Moreover, we explore how acid concentration and ionic strength influence collision frequency and signal detectability. Collectively, our work establishes a more rigorous framework for understanding single-particle HER electrocatalysis and H absorption on Pd, providing new mechanistic insights beyond conventional collision models.

2 Experimental

2.1 Palladium Nanoparticle synthesis

The synthesis was carried out mainly according to the method provided by Park et al.[63, 68] About 1.77 mg of $PdCl_2$ was completely dissolved in 20 mL of 1 mM HCl in a round bottom flask under sonication for 1 hour. An oil bath was preheated to 95°C and the flask was covered by aluminum foil and set into the oil bath. While then, about 3.842 mg of citric acid was added into the solution under vigorous stirring. After 5 minutes of reflux, the flask was immediately removed from the heating and 2 mL of 0.1 M $NaBH_4$ was added dropwise. The color of the solution turned from light yellow to brown. After cooling down, the NP solution was transferred to a centrifuge tube to centrifuge for 30 minutes at 2000 rpm. This process was repeated once, and only the supernatant was collected after each centrifuge. We observed a little amount of black solid at the bottom of each centrifuge tube. Then, the solution was transferred to a disposable glass vial for future use. A aliquot of NP solution was used for DLS charatcterization.

2.2 Carbon Fiber electrode fabrication

A single 5 μm diameter carbon fiber was put in to a 1.2, 0.66 mm diameter glass capillary. Then, the glass capillaries were pulled with a P-97 pipette puller, and the extra carbon fiber was cut off at its intersection with the glass tip. After that, the pipette tips were immerged into epoxy for 10 minutes and moved to an oven to dry for at least 2 hours. A tungsten wire with some silver epoxy was put into the capillary from the other end and fixed by another epoxy. The electrodes were moved to the oven to dry for at least 90 minutes. The carbon fiber electrodes were then characterized in 1 mM FcMeOH solution with cyclic voltammetry. A chlorinated silver wire was used as a quasi-Ag/AgClreference electrode.

2.3 Palladium Electrodeposition on Carbon Fiber Electrode

The Pd-electrodeposited carbon fiber electrode (CFE) was prepared using a previously fabricated CFE following the aforementioned procedure. To prepare a 1 M NH_4Cl solution, 0.5349 g of NH_4Cl was dissolved in 10 mL of nanopure water. Subsequently, 0.709 mg of $PdCl_2$ was added to 4 mL of this solution to obtain a 1 mM $PdCl_2$ solution. The mixture was subjected to sonication for at least 30 minutes to ensure complete dissolution of the Pd salt. Finally, the solution was diluted twofold prior to electrodeposition.

The cyclic voltammogram (CV) of the bare carbon fiber electrode (CFE) prepared for electrodeposition was first

recorded in 0.1 mM perchloric acid, the same electrolyte used in the NP collision experiments. Subsequently, CV for electrodeposition was conducted from 0.8 V to -0.6 V at a scan rate of 20 mV/s, initiating at 0 V and scanning in the negative direction. Following this, electrodeposition was performed via CV cycling between 0.2 V and -0.6 V, starting from 0 V in the negative direction, for a total of 15 cycles. Finally, the Pd-deposited CFE was transferred back into the same perchloric acid solution for post-deposition CV measurements.

2.4 Pd NP Collision

An aliquot of the stock Pd NP solution was transferred into a low-binding tube at the beginning of each experimental day and briefly sonicated for 2–3 seconds. Subsequently, 4 mL of perchloric acid solution and 60 μL of the sonicated Pd NP dispersion were added to a 6 mL disposable glass vial. The mixture was homogenized by rapid pipetting and gentle shaking. The vial was then securely placed in a Faraday cage. A carbon fiber electrode (CFE) was freshly polished, rinsed with nanopure water, and immediately immersed into the prepared solution. Separately, a freshly chlorinated silver wire was removed from the bleach, thoroughly rinsed with nanopure water, dried with compressed air, and inserted into the solution to serve as the reference electrode, before applying any potential. Under each condition, the same experiments were repeated at least three times to guaranttee the reproducibility.

3 Results

3.1 Palladium Nanoparticle synthesis and characterization

The NPs synthesized with the method in the experimental part are characterized with DLS. The stability of the NP was also investigated with DLS. The NP concentration used in this part was identical to that of the NP concentration in all collision experiments. As shown in **Figure 2**, the intensity mean diameter of NPs dispersed in nanopure water was around 56.2 nm, much larger than the desired size, 10-15 nm, reported by the authors. [63, 68] Despite this, the average Polydispersity Index (PDI) was 0.347, so the NPs are not very monodisperse in nanopure water. After 10 minutes, both NPs in the 0.1 mM perchloric acid aggregated, with or without additional electrolyte. However, the diameters of NPs in these two solutions are slightly different. When the supporting electrolyte presents, the intensity mean diameter was 247.3 nm, but when the electrolyte are absent, the intensity mean diameter was 216.7 nm. In contrast, NPs in the 0.01 mM $HClO_4$ + 20mM $NaClO_4$ and in the 20mM $NaClO_4$ solution did not undergo severe aggregation. Even so, the size distribution became wider when more electrolyte was present than when the supporting electrolyte was absent. It is obvious that NPs cannot grow suddenly from 48 nm to 200 nm, so the size distributions of

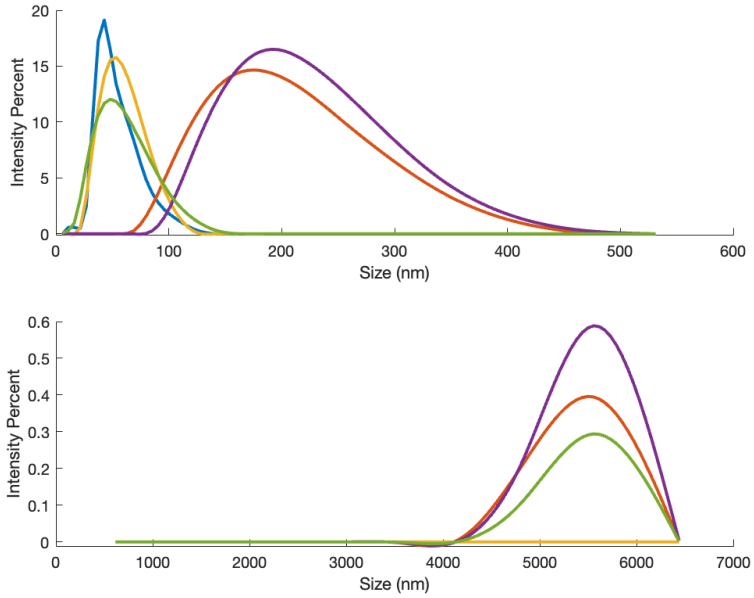

Figure 2: DLS size distributions of Pd NPs in different solution conditions. The size distributions vary based on the composition of the dispersing medium, including 1:100 dilution in nanopure water (blue), 0.1 mM $HClO_4$ (red), 20mM $NaClO_4$ (yellow), 0.1 mM $HClO_4$ + 20mM $NaClO_4$ (purple), and 0.01 mM $HClO_4$ + 20mM $NaClO_4$ (green). The observed shifts in peak size and distribution width indicate the influence of electrolyte composition on NP aggregation and stability.

single measurements were plotted out to observe any aggregation during the measurements. In this case, each single measurement involves 15 runs, and each run spent 10s. The first measurement started at 600 s and ended at 750 s. The size distribution (**Figure 3**) indeed shifted over time. However, when I examined the distribution of collision peaks and steady state current overtime, the hydrogen evolution current and the adsorption charge transfer indicated that the size of NPs colliding with the electrode remained unchanged.

3.2 Electrodeposition and CV of HER

Before doing NP collision, we first performed CV of HER on Pd in 25 mM acid to test our system and to identify the most important potential window for NP collision. Firstly, it should be noted that the actual precursor of our electrodeposition of Pd onto the CFE was actually $[PdCl_4]^{2-}$,(Equation 18) as Pd(II) readily forms a soluble and stable complex in aqueous solution of chloride, and this is also the reason why we added hydrochloric acid when we synthesize Pd NPs.[69–71]

$$PdCl_2 + 2Cl^- \rightarrow [PdCl_4]^{2-} \tag{18}$$

$$[PdCl_4]^{2-} + 2e^- \rightarrow Pd^0 + 4Cl^- \tag{19}$$

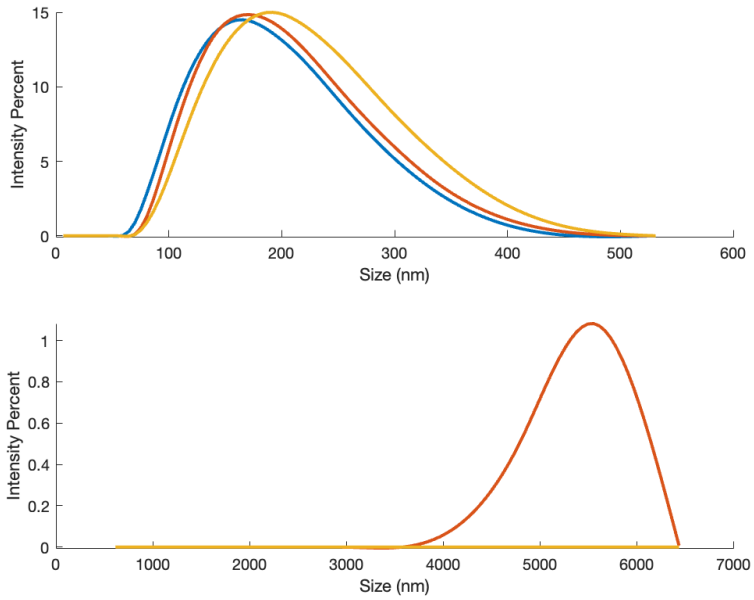

Figure 3: Dynamic Light Scattering (DLS) size distributions of Pd NPs at different time points. The top panel shows the primary size distributions at about 750s (blue), 900s (red), and 1050s (yellow), illustrating the evolution of NP sizes over time. The curves indicate a slight shift towards larger sizes, suggesting minor aggregation or growth of Pd NPs. The bottom panel presents an extended size distribution, suggesting that the second peak at larger size is likely due to random error.

The cyclic voltammogram shown in **Figure 4** from −0.6 V to +0.8 V (vs. Ag/AgCl) clearly exhibits a rising cathodic current between approximately 0 V and −0.6 V, indicating the electrodeposition of Pd onto the electrode surface. A small anodic peak appears around −0.3 V, followed by a prominent anodic peak near +0.5 V. We attribute this large anodic peak to the complete oxidation of the previously deposited Pd. Bravo-Rodriguez et al. also reported a similar CV in 1 mM Pd(II) and 1 M NH_4Cl solution.[70] In another attempt, (**Figure S1**) we observed that this peak was split into a doublet. A similar phenomenon was reported by Rezaei et al., who attributed the doublet to the oxidation of different Pd species. According to their interpretation, the peak at approximately 0.5 V corresponds to the oxidation of palladium hydride (PdH_x), while the peak near 0.6 V corresponds to the oxidation of metallic Pd. By performing multiple consecutive voltammetric cycles, they found that the peak at 0.6 V gradually diminished, which they attributed to the increasing formation of PdH_x over time, leading to the suppression of the metallic Pd signal [69].

The integrated charge of the anodic peak was measured to be 195.334 nC, corresponding to approximately 6.09×10^{11v} Pd atoms deposited on the electrode surface. For an electrode with a radius of approximately 2.5 μm, this quantity of Pd atoms would be sufficient to form a full monolayer, thus effectively mimicking a planar Pd ultramicroelectrode (UME). However, it is important to note that during electrodeposition, Pd atoms tend to nucleate and form clusters, eventually aggregating into NPs adhered to the electrode surface.[72] A uniform, surface-covering

Pd film can only be achieved when either the number of NPs is sufficiently large or the particles themselves grow large enough to coalesce across the electrode surface.

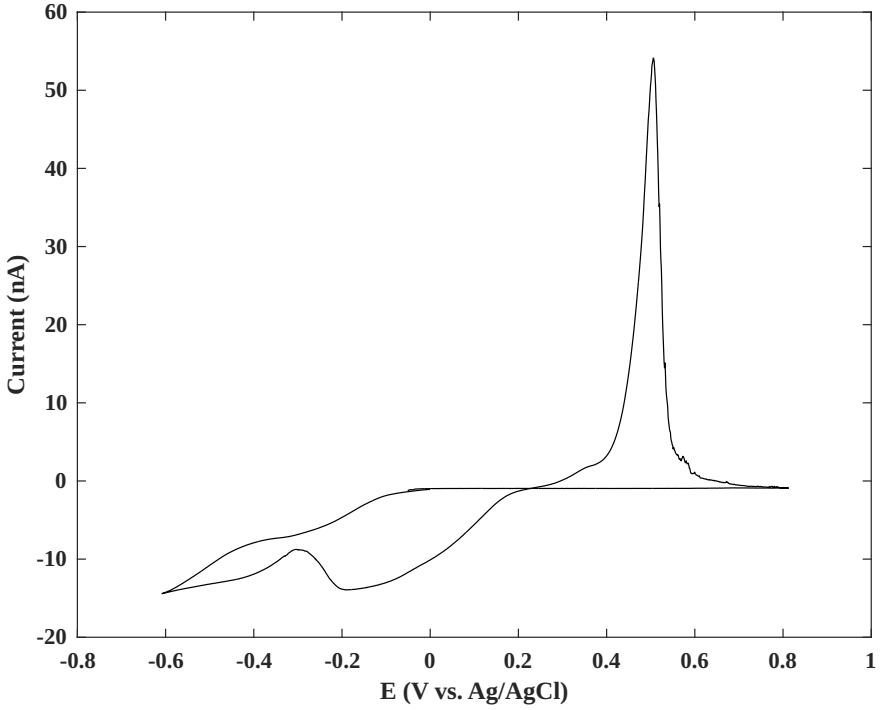

Figure 4: Cyclic voltammogram of Pd deposition and oxidation. The current increase from -0.4 V to -0.6 V indicates Pd deposition, with a small anodic peak at -0.22 V and a significant anodic doublet at +0.6 V corresponding to Pd oxidation.

A smaller anodic peak consistently appeared around −0.2V in the CVs. While Bravo-Rodriguez et al. did not assign this feature, we attribute it to hydrogen desorption from the Pd surface. This assignment is supported by HER CVs performed in highly dilute perchloric acid (0.1mM), where the same peak persisted and exhibited a scan-rate-dependent response. Notably, the peak current increased approximately with the square root of the scan rate, suggesting that the process is not purely surface-limited but involves subsurface hydrogen diffusion (**Figure S2**).To ensure full Pd coverage on the carbon fiber electrode (CFE) and avoid undesired Pd oxidation, we performed 15 cycles of CV scans from −0.6 V to 0.2 V. During these cycles, a cathodic peak around −0.35 V emerged and was followed by a steady-state region, likely reflecting diffusion-limited reduction of Pd^{2+} ions near the electrode. As the deposition progressed, the anodic peak near −0.2 V gradually intensified and split into a doublet, while its onset and end potentials remained largely unchanged. This behavior suggests structural evolution of the Pd surface during growth: initially deposited Pd exhibited weaker interaction with hydrogen, while later-deposited Pd with different crystallographic facets or surface arrangements exhibited stronger H-binding affinity. Consequently, the doublet feature likely arises from coexisting Pd domains with distinct hydrogen desorption characteristics. This interpretation is further supported by the similar doublet anodic features observed in multicycle deposition CVs (**Figure 5**). Quantitative analysis further revealed that

the integrated area of this anodic peak increases nearly linearly with the number of deposition cycles, indicating a proportional increase in the amount of desorbed hydrogen and thus a steady expansion of the electrochemically active Pd surface and volume (**Figure S4**).

Then, with this freshly deposited Pd-CFE, we scanned a CV in 25 mM perchloric acid, initially from 0 V negatively toward –1.6 V, as shown in **Figure 6a–b**. We observed that between approximately –0.3 V and –0.4 V, the cathodic current began to increase, reaching a plateau until about –0.7 V. Beyond this point, the current dropped sharply, reaching –800 nA near –1.6 V vs. Ag/AgCl.

To further analyze the hydrogen evolution kinetics, we identified two regions on the CV where the overpotential η and $\log_{10}(|I|)$ displayed clear linear relationships, as expected from the Tafel equation (Equation 26). Based on the conversion between potential and overpotential discussed in **Appendix A**, we assumed that $E = -0.5$ V corresponds to an overpotential $\eta \approx -0.2$ V in 25 mM $HClO_4$.

Tafel analysis of the hydrogen evolution reaction (HER) was performed on two linear segments of the cyclic voltammogram ($\eta \in [-0.3, -0.2]$ V and $\eta \in [-0.7, -0.6]$ V), as shown in **Figure 6c–d**, yielding Tafel slopes of 382.5 mV/dec ($\alpha = 0.1546$) and 137.0 mV/dec ($\alpha = 0.4318$) with $R^2 > 0.998$, calculated using Equation 15. At low overpotentials ($E = -0.5$ V to -0.6 V), the HER exhibits very slow kinetics, with $\alpha = 0.1546$ indicating an asymmetric energy barrier and a high Tafel slope, suggesting a possible change in the rate-determining step. In contrast, at high overpotentials ($E = -0.9$ V to -1.0 V), the reaction shows faster kinetics, with $\alpha \approx 0.5$, consistent with a symmetric Volmer–Heyrovsky mechanism. Furthermore, a very moderate current plateau in the range $E = -0.4$ V to -0.7 V was observed, which reveals that the total current was significantly limited in this potential range, likely due to the absorption of surface adsorbed hydrogen into the Pd layer, rather than its recombination to molecular hydrogen. This absorption-dominated regime effectively diverts H_{ads} away from the HER pathway, thereby diminishing the observable faradaic current associated with H_2 evolution. As a result, the Tafel slope extracted from this potential window appears artificially steep, not due to increased activation energy, but due to the reduced contribution of the HER branch to the net current. A similar distortion of the Tafel slope was also reported by Wan et al. on Pt electrodes with high catalyst loading, where the accumulation and reoxidation of H_2 led to a suppression of the net HER current. Although the underlying mechanisms differ — gas-phase product buildup in the Pt system versus bulk hydrogen absorption in Pd — both phenomena result in an steep Tafel slope due to diversion or offset of surface-adsorbed hydrogen.[15]

To confirm the intrinsic reaction mechanism under minimal interference, we repeated the experiment in 0.1 mM acid, where a clear linear Tafel region was observed with a slope of approximately 30 mV/dec (**Figure S3**). This value is characteristic of a Tafel-type hydrogen evolution pathway, where two adsorbed hydrogen atoms recombine to form molecular hydrogen. These results suggest that, under low-overpotential conditions and in the absence of

significant absorption or transport limitations, the Tafel step can dominate the reaction kinetics. Notably, a similar kinetic signature was later observed in the NP collision experiments, reinforcing this mechanistic assignment.

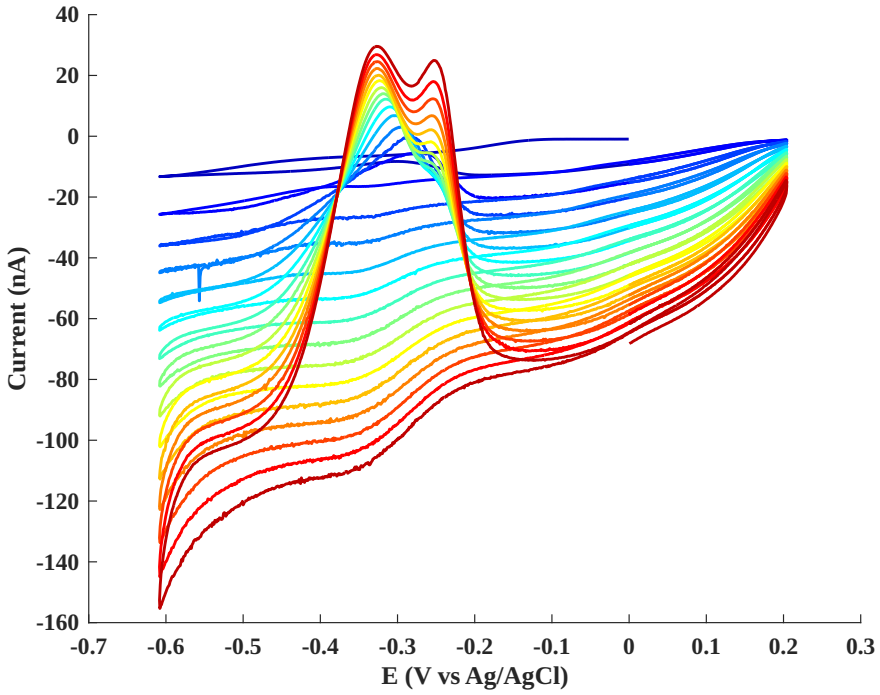

Figure 5: Cyclic voltammogram of Pd deposition with 15 cycles. The cathodic current and anodic peaks increased over time, indicating an increase in the surface area and reactivity during the deposition. The bluer curve represents the first cycle and the red curve is the last cylce, accordingly.

Another noteworthy thing is that although we are unable to observe the hydrogen desorption in the 25 mM acid, from **Figure S2**, we also noticed that the anodic peak for H desorption increases with scan rate, and the potential of the peak also shifts accordingly. We then fitted the peak current (I_p) and peak potential (E_p) with the square root of scan rate ($\sqrt{v}$) and $\log_{10}(v)$, respectively, and found, as illustrated in **Figure S2 c**, that the peak current scales linearly with $\sqrt{v}$, at least till the scan rate reached 20 mV/s, suggesting diffusion-controlled behavior, while the peak potential exhibits a linear dependence on $\log_{10}(v)$, consistent with the Laviron model.

$$E_p = E^0 + \frac{RT}{\alpha n F} \ln\left(\frac{RT}{\alpha n F} \cdot \frac{k^0}{v}\right) \tag{20}$$

This indicates that the hydrogen desorption process on Pd involves quasi-reversible electron transfer kinetics. Details of the kinetic parameter extraction are provided in **Appendix B**. The kinetic parameters, α and k^0, extracted from the anodic peak using Laviron analysis, are 0.23 and 3.65 s^{-1}, respectively, corresponding to the electron-transfer-limited desorption step ($H_{ads} \rightarrow H^+ + e^-$). These values indicate that hydrogen desorption on Pd is both kinetically slow and electrochemically asymmetric. The low α reflects a weak dependence on overpotential and a high activation barrier for

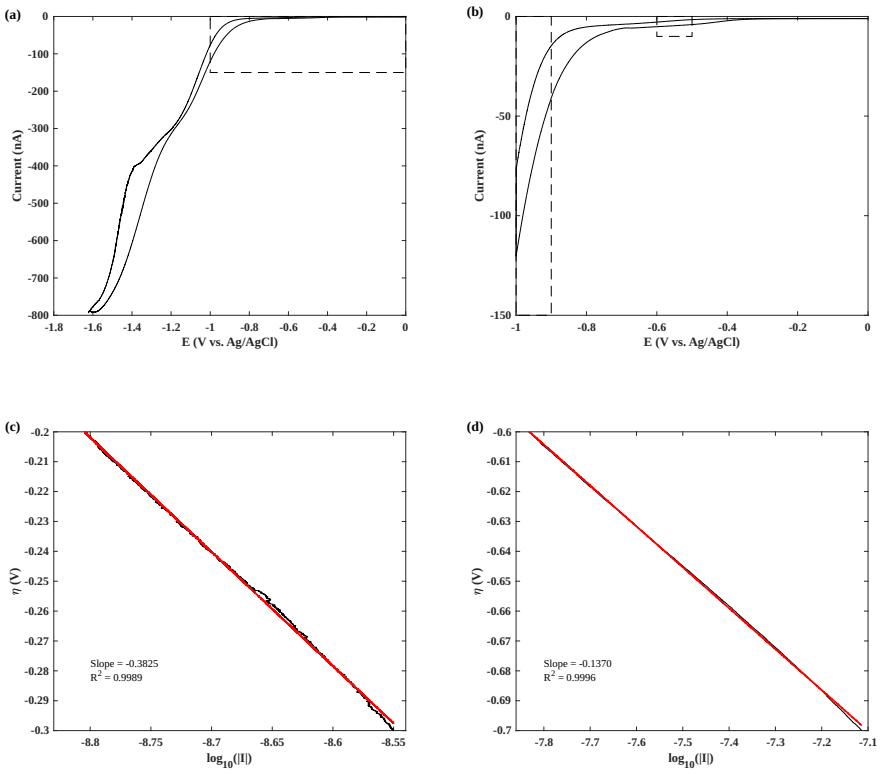

Figure 6: (a) Full cyclic voltammogram of Pd electrode under HER conditions. (b) Zoomed-in view from –1 to 0 V, with Tafel analysis regions marked by dashed boxes. (c,d) Tafel plots corresponding to η = –0.3 –0.2 V and η = –0.7 –0.6 V, respectively. Linear fit results are shown in red. The cyclic voltammogram was taken in a 25mM perchloric acid.

electron transfer in the oxidative direction. Meanwhile, the modest k^0 is consistent with slow desorption kinetics, likely due to the strongly negative hydrogen adsorption free energy on Pd surfaces. Assuming a diffusion layer thickness of $\delta = 2.36\ \mu$m at 0.3 ms and a proton concentration of 25 mol/m^3, this rate constant translates to an interfacial value of approximately 3.45×10^{-7} m/s. This further implies that the reverse reaction—hydrogen adsorption—is kinetically facile. Therefore, any observation suggesting that adsorption is the rate-determining step should instead be attributed to the subsequent absorption of hydrogen into the Pd lattice.

3.3 Nanoparticle Collision with HER

3.3.1 Observation of Current Transients

Most observed current transients consist of two components: an initial peak followed by a gradual stabilization of the current, as shown in **Figure 8**. These features correspond to distinct electrochemical processes involved in the HER, with the sharp initial peak attributed to rapid hydrogen adsorption (Volmer step) and the subsequent stabilization

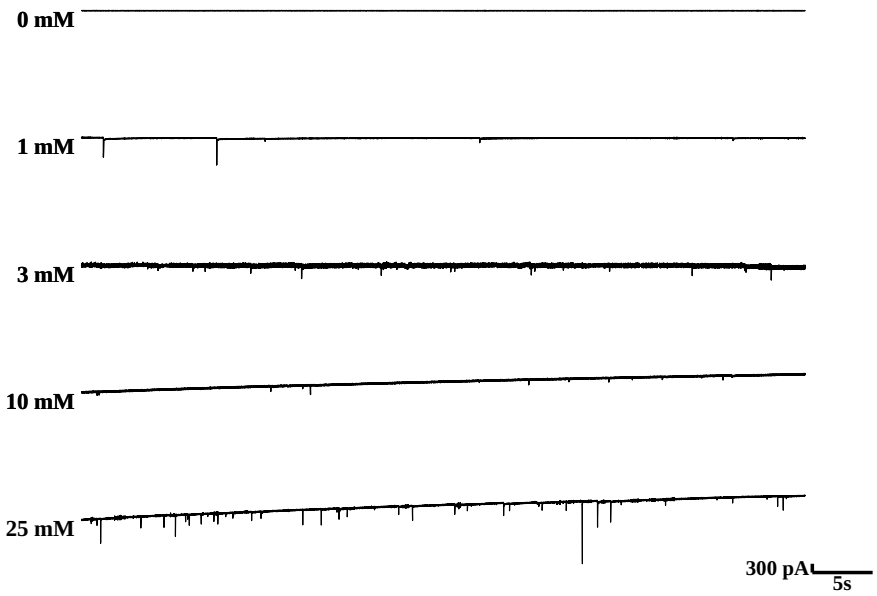

Figure 7: Representative traces of Pd NP collisions at varying $HClO_4$ concentrations at 0 mM, 1 mM, 3mM, 10mM, 25mM. Chronoaperograms were recorded at -0.7 V vs. Ag/AgCl.

reflecting hydrogen evolution via the Heyrovsky and Tafel steps.[37] Notably, unlike the work of Defnet et al., who employed a 10 kHz low-pass filter to temporally resolve hydrogen adsorption and evolution dynamics on Pt NPs,[37] we successfully distinguished these two processes using a lower filter frequency of 2 kHz. This observation indicates that the kinetic separation between hydrogen adsorption and hydrogen evolution on Pd NPs is sufficiently pronounced under our experimental conditions. The broader temporal window between the Volmer and Heyrovsky steps suggests that HER kinetics on Pd are intrinsically slower than on Pt, enabling clear distinction between adsorption and evolution even under reduced bandwidth conditions. Furthermore, the use of a lower filter frequency substantially reduced background noise levels, allowing experiments to be conducted under more challenging conditions, such as lower acid concentrations, smaller overpotentials, and smaller NP sizes, without the risk of collision peaks being obscured by noise.

Interestingly, under sufficiently high overpotential and proton concentration conditions, we frequently observed that following the initial adsorption peak, the current transient exhibited a gradual decay before reaching a new quasi-steady baseline, rather than displaying a classical staircase-like step increase. This behavior suggests that Pd NPs remain adhered to the electrode surface after impact and continue catalyzing HER. However, as hydrogen coverage on the Pd surface increases and subsurface PdH_x form, the catalytic activity decreases relative to the initial collision event, leading to a lower but sustained steady-state current.

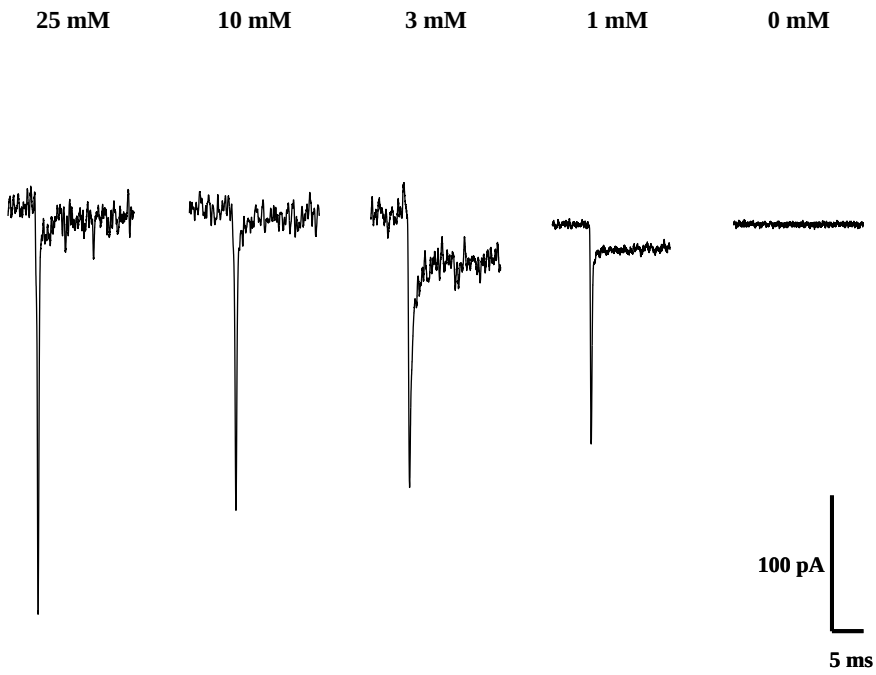

Figure 8: Representative single peaks due to single Pd NP collision. Current transients of Pd NP collisions at varying $HClO_4$ concentrations, showing initial peaks (Volmer step) followed by staircase currents (Heyrovsky step+ Tafel step). Chronoaperograms were recorded at -0.7 V vs. Ag/AgCl.

3.3.2 Concentration Dependence Study

To further characterize these transient features, we analyzed three key parameters: (1) the peak width at half height, (2) the integrated area of the peak, and (3) the quasi-steady current plateau. As shown in **Figure 9a**, the peak width decreases as the acid concentration increases, reaching a plateau at approximately 3 mM. This trend suggests that at low proton concentrations, mass transport limitations broaden the transient response, while at higher concentrations, the intrinsic hydrogen adsorption kinetics dominate the timescale. Since the electron supply from the electrode is abundant under the applied potentials, variations in acid concentration primarily affect the proton availability near the NP surface, influencing the proton-coupled electron transfer (PCET) processes.

A similar phenomenon was observed by Defnet et al.[37] for Pt NPs using a microjet-assisted setup. Compared to their results, the peak width in our experiments varied more gradually, from approximately 0.34 ms to 0.27 ms, whereas in the microjet system, the width rapidly decreased from about 0.2 ms to 0.04 ms as the proton concentration increased. This difference can be attributed to the distinct mass transport environments: in the microjet setup, forced convection strongly enhances proton delivery to the NP surface and accelerates the adsorption kinetics, whereas in our diffusion-controlled system without external convection, proton transport is governed purely by diffusion. Notably, when Defnet et al. suppressed convection in their system, the half-widths measured under comparable acid concentrations (0.25

ms) were very close to those observed in our experiments, further validating that our measurements reflect intrinsic diffusion-limited adsorption dynamics.

It is important to note that the theoretical time resolution of our system, determined by the 2 kHz low-pass filter, is 0.187 ms (see **AppendixD**). In most cases, the measured peak widths are significantly larger than this limit, confirming that the use of a 2 kHz filter does not compromise the temporal resolution of the observed transients.

The second parameter of interest is the integrated area of the peak, which corresponds to the total charge transferred during the transient event. According to Faraday's law, the integration of current over time reflects the number of protons adsorbed onto the NP surface during the Volmer step of the HER. As shown in **Figure 9b**, the integrated charge increases with acid concentration initially but eventually reaches a plateau. This behavior is consistent with prior observations on NP systems, where surface hydrogen adsorption becomes saturated beyond a certain proton concentration.

In the case of Pt nanoparticles, such saturation behavior can typically be attributed to the formation of a complete hydrogen monolayer on the surface. However, for Pd nanoparticles, the situation is fundamentally different. Unlike Pt, Pd can absorb hydrogen not only on its surface but also into its bulk lattice, enabling much greater hydrogen uptake beyond monolayer adsorption. Additionally, while commercial Pt NPs are often highly mesoporous—resulting in electrochemically active surface areas (ECSA) that significantly exceed geometric estimates—there is no evidence of substantial mesoporosity in the Pd NPs synthesized by the methods referenced herein.[63, 68]

Moumaneix et al. reported that hydrogen surface adsorption on Pd saturates at approximately 0 V vs. RHE, which corresponds to about –0.291 V vs. Ag/AgCl in 25 mM $HClO_4$.[73] This is much more positive than the applied potential of –0.7 V vs. Ag/AgCl used in our experiments, where adsorption should be complete. Based on a reported surface charge density of 240 $\mu C/cm^2$ for monolayer hydrogen adsorption on Pd,[74] the theoretical charge for a 56 nm spherical Pd NP is estimated to be approximately 23 fC. In contrast, the experimentally measured charge at –0.7 V is 80 fC—more than three times this value. If we assume full surface coverage, this implies an apparent surface roughness factor of 3.43. However, since the Pd NPs used here are not mesoporous and do not exhibit significant roughness or high-curvature features, the excess charge is more plausibly attributed to bulk hydrogen absorption rather than an expanded surface area. This strongly supports the interpretation that, under the applied conditions, hydrogen penetrates into the Pd lattice beyond monolayer surface adsorption.

These observations strongly suggest that the saturation behavior observed in **Figure 9b** does not arise solely from surface adsorption. Rather, it reflects a combination of surface adsorption and bulk absorption of hydrogen into the Pd lattice. The appearance of a plateau in the integrated charge at a given applied potential further supports this

interpretation, implying that hydrogen absorption in Pd NPs is primarily governed by the electrochemical driving force—the applied potential. Once hydrogen saturation is achieved, further increases in proton concentration do not significantly enhance hydrogen absorption into the Pd lattice, indicating that the absorption process is largely potential-driven rather than concentration-driven under the investigated conditions. Since the transition from adsorbed to absorbed hydrogen does not involve an additional electron transfer step, the excess hydrogen is incorporated into the Pd lattice via a single Faradaic process corresponding to the Volmer step.

This interpretation is further supported by estimates of the hydrogen diffusion in Pd. Based on first-principles path-integral molecular dynamics simulations, the hydrogen diffusion coefficient in unstrained Pd at 298 K is approximately $1.27\times10^{-6}\,\mathrm{cm}^2/\mathrm{s}$.[75] This value is consistent with experimental measurements in Pd thin films, which report diffusion coefficients on the order of $10^{-6}\,\mathrm{cm}^2/\mathrm{s}$ at room temperature.[76] Given the small size of the NPs (56 nm diameter), the characteristic diffusion time can be estimated by $t \sim r^2/D$, where r is the NP radius. Substituting $r = 28\,\mathrm{nm}$ and $D = 1.27 \times 10^{-6}\,\mathrm{cm}^2/\mathrm{s}$, we find that hydrogen can diffuse across the entire NP within approximately 6 μs. This timescale is much shorter than the typical peak duration observed in our experiments, indicating that hydrogen absorption is not limited by hydrogen diffusion in the Pd NP. This also means that we are not able to distinguish hydrogen adsorption and hydrogen evolution on single NPs.

Therefore, the saturation of hydrogen uptake cannot be attributed to mass transport limitations or surface site saturation alone. Before concluding that the process is kinetically limited, it is essential to consider whether a thermodynamic limit has been reached. Specifically, hydrogen absorption into the Pd lattice may attain a quasi-equilibrium condition, governed by the balance between the electrochemical potential of protons in the electrolyte and the chemical potential of hydrogen within the Pd lattice. In electrochemical terms, the latter can be expressed as:

$$\mu_{\mathrm{H,Pd}}(x) = \mu^0_{\mathrm{H,Pd}} + RT \ln\left(\frac{x}{1-x}\right) \tag{21}$$

where x denotes the fractional occupancy of available interstitial sites. The electrochemical potential of solvated protons and electrons at the electrode interface is given by:

$$\tilde{\mu}_{\mathrm{H^+}} + \mu_{\mathrm{e^-}} = \mu^0_{\mathrm{H^+}} + RT \ln a_{\mathrm{H^+}} - eE \tag{22}$$

where E is the applied electrode potential (vs. reference), and $a_{\mathrm{H^+}}$ is the proton activity.

At equilibrium, the chemical potential of absorbed hydrogen in Pd matches the electrochemical potential of protons and electrons:

$$\mu_{\mathrm{H,Pd}}(x) = \tilde{\mu}_{\mathrm{H^+}} + \mu_{\mathrm{e^-}} \tag{23}$$

This equation imposes a strict thermodynamic limit on the maximum hydrogen fraction x achievable within the Pd NPs at a given applied potential.

Under the overpotentials employed in this study (e.g., −0.7 V vs. Ag/AgCl), the equilibrium condition theoretically permits a near-complete hydrogenation of the Pd lattice (i.e., $x \approx 1$), as shown in **Appendix E**. However, the experimentally measured hydrogen absorption, derived from the integrated charge, corresponds to only a small fraction of the theoretical maximum ($x \approx 0.08$), as shown in **Appendix F**. This discrepancy indicates that, although hydrogen can rapidly diffuse throughout the NP bulk, the overall absorption process is kinetically limited at the surface, preventing full occupation of available interstitial sites. Consequently, once a potential-controlled quasi-equilibrium is established, the total amount of absorbed hydrogen—and thus the integrated charge—becomes largely independent of further increases in proton concentration. A more detailed kinetic analysis is provided through the potential dependence study discussed in the next section.

Furthermore, the third parameter of interest is the quasi-steady-state current. In cases where NPs remain adhered to the electrode surface and continue to catalyze the HER, the measured current gradually approaches a quasi-steady-state value. This steady-state current can be estimated using Equation (16), assuming diffusion-controlled proton supply to a spherical Pd NP. For a 56 nm diameter Pd NP in 25 mM $HClO_4$, the theoretical steady-state current is calculated to be approximately 5.48 nA.

It is important to note that this estimation assumes ideal conditions, including a fully clean and catalytically active NP surface. In practice, the NP surface may undergo partial passivation (e.g., oxide formation) or contamination (e.g., adventitious adsorption of impurities), both of which can reduce the effective electrochemical active area and suppress catalytic activity. Consequently, we often observe only a transient peak without a subsequent staircase-like response. Even when a staircase was observed (**Figure 10**), the measured quasi-steady-state current remained significantly lower than the theoretical value.

Moreover, according to the steady-state diffusion model, $i_{\mathrm{ss}} \propto C$, the current is expected to increase linearly with proton concentration. However, our experiments revealed that the quasi-steady-state current remained nearly constant across the investigated concentration range. These observations suggest that under the applied potential of –0.7 V vs. Ag/AgCl, the HER is not limited by mass transport of protons to the NP surface. Instead, the reaction rate is likely limited by the intrinsic hydrogen evolution kinetics on Pd, or by competing processes such as hydrogen absorption into the Pd lattice, which consume surface-adsorbed hydrogen and diminish the net HER rate.

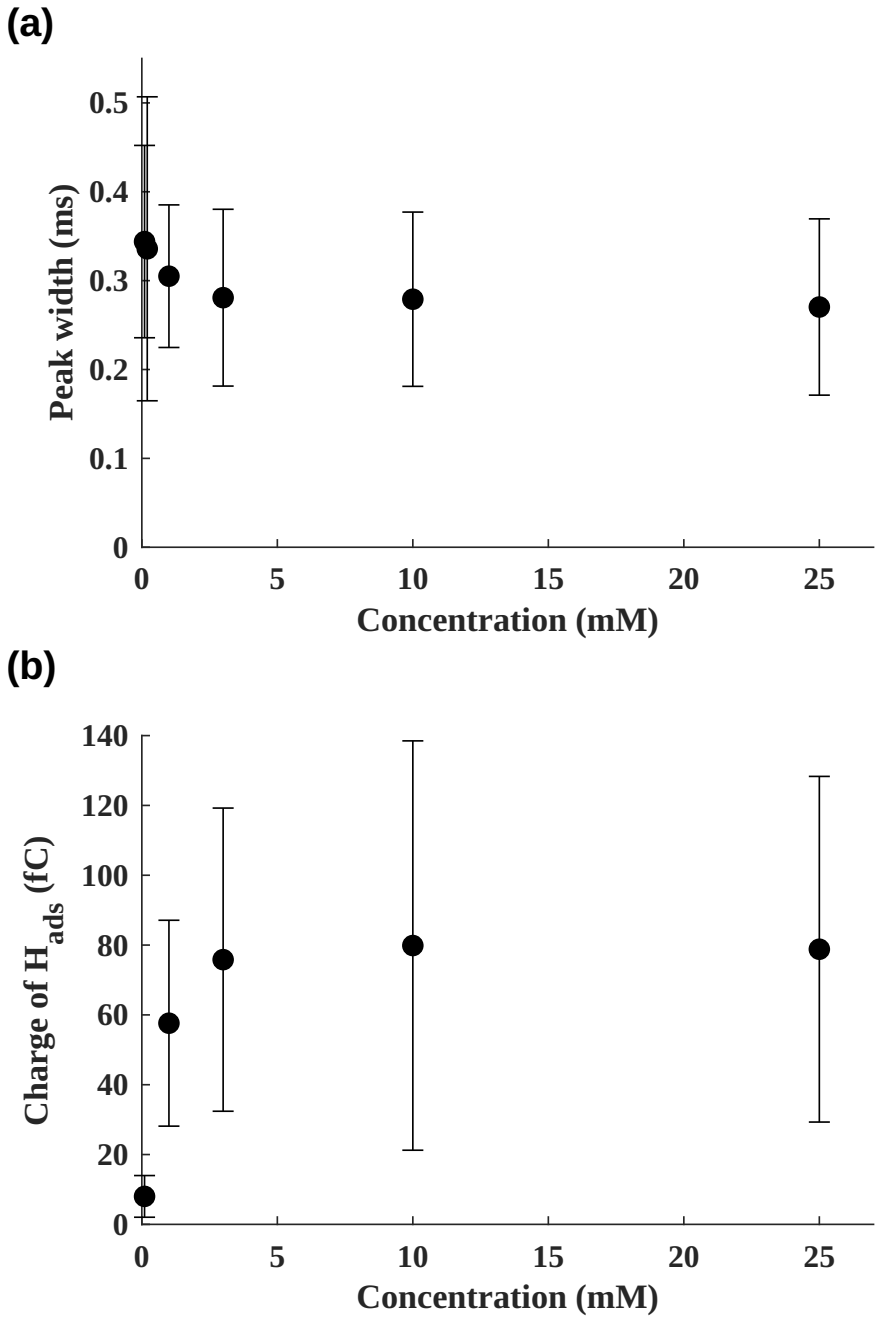

Figure 9: (a) Peak width decreases with increasing $HClO_4$ concentration, reflecting faster hydrogen adsorption kinetics at higher proton availability. (b) Total charge associated with adsorbed hydrogen increases with acid concentration, indicating more complete surface coverage or partial hydrogen absorption at higher $[H^+]$. Chronoaperograms were recorded at -0.7 V vs. Ag/AgCl.

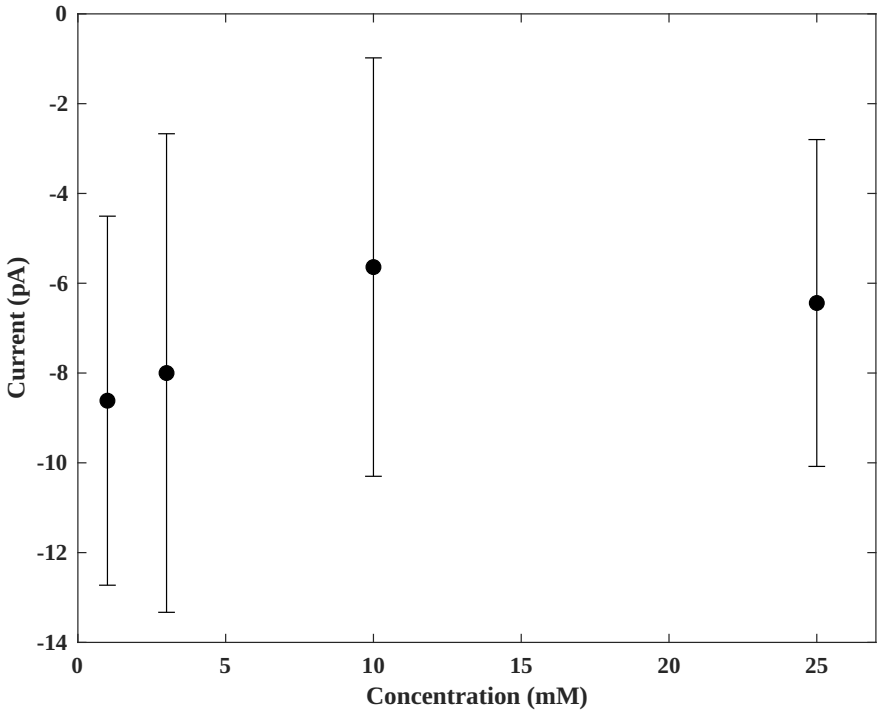

Figure 10: The quasi-steady state current remains constant with increasing $HClO_4$ concentrations, revealing that this current is not limited by concentration. Chronoaperograms were recorded at -0.7 V vs. Ag/AgCl with 60 uL Pd NP solution added.

3.3.3 Potential dependence study

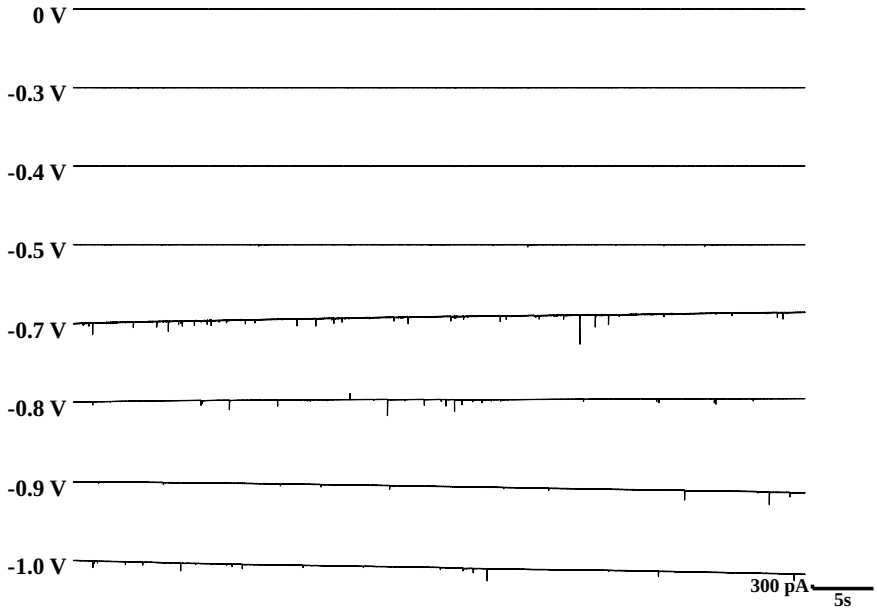

Figure 11: Representative traces of Pd NP collisions at varying potential at 0 V, -0.3 V, -0.4 V, -0.5V, -0.7 V, -0.8V, -0.9V, -1.0V Chronoaperograms were recorded in a 25 mM $HClO_4$ solution with 60 uL Pd NP solution added.

To achieve a better understanding of hydrogen evolution and hydrogen absorption on Pd NPs under varying conditions, we conducted a potential-dependent study. Pd NP collision experiments were performed at a series of increasingly negative potentials to evaluate how the applied driving force influences the reaction pathway. As shown in **Figure 12**, at low overpotentials (–0.4 V vs Ag/AgCl), the hydrogen adsorption peak is barely detectable. As the overpotential increases, however, the peak height rises rapidly, reaching approximately 400 pA on average. Not limited by this initial observation, we analyzed the half width, peak area, and baseline change of the collision events.

We first analyzed the half-width of individual peaks, revealing that the peak half-width fluctuates only minimally over the potential range from 0 V to –1.0 V.(**Figure 13b**) This indicates that the time for NPs to complete hydrogen absorption does not remains constant with increasing overpotential, which is different from the behavior observed on Pt NPs by Defnet et al.[37] This behavior suggests that the Volmer step on Pd NPs is limited by a process with weak potential dependence.

Moreover, the integrated peak area increases continuously with increasing overpotential, without any sign of saturation—a marked contrast to Pt surfaces, where hydrogen adsorption saturates at monolayer coverage and the integrated area plateaus as the potential becomes more negative (**Figure 13a**). Although increasing proton concentration can eventually saturate hydrogen absorption on Pd, simply increasing the overpotential does not induce such saturation. Based on the integrated peak area, we estimated the hydrogen content x in PdH_x at different potentials. Assuming

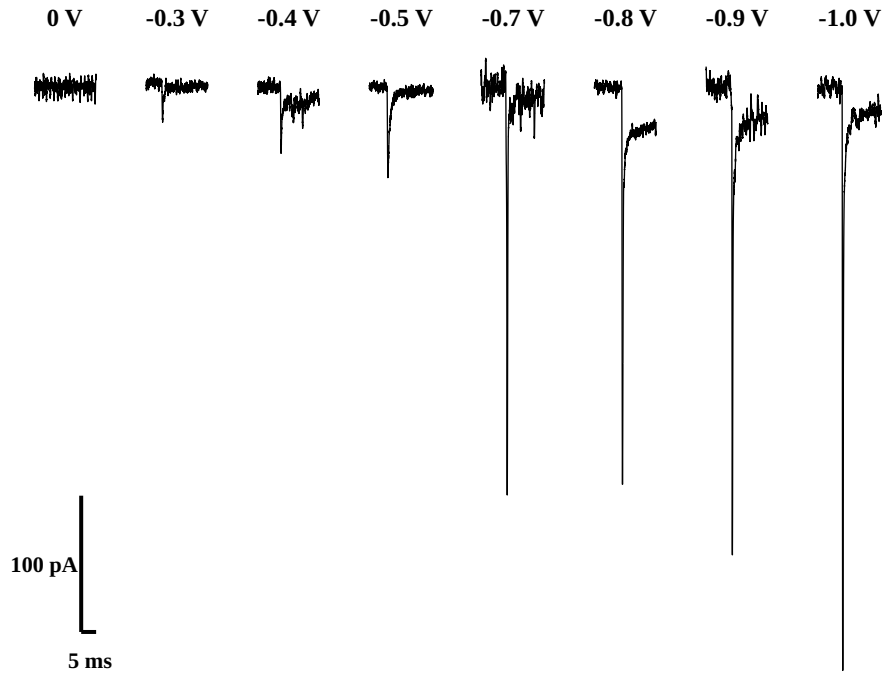

Figure 12: Representative peaks of Pd NP collisions at varying potential at 0 V, -0.3 V, -0.4 V, -0.5V, -0.7 V, -0.8V, -0.9V, -1.0V Chronoaperograms were recorded in a 25 mM $HClO_4$ solution with 60 uL Pd NP solution added.

the theoretical full capacity corresponds to a charge transfer of 1001 fC per Pd NP, we found that at –0.7 V, x was approximately 0.08, and as the potential reached –1.0 V, x rose to around 0.134. This range falls within the reported $\alpha - \beta$ phase transition region in PdH_x (typically observed for x between approximately 0.03 and 0.6).[77]

Finally, to provide additional insight into the kinetic processes involved, we analyzed the changes in baseline current before and after collision events and fitted these data using various kinetic models, following the approach of Defnet et al.[37] On platinum, the HER is widely accepted to be rate-limited by the Heyrovsky step, as supported by both experimental and theoretical studies.[37, 78] However, for our citrate-capped Pd NPs, the HER kinetics appear to be more complex, particularly at low overpotentials, and deviate significantly from a simple Heyrovsky-limited mechanism. We first considered and subsequently excluded the Volmer step as the possible rate-determining step (RDS), based on both poor fitting quality and unphysically low extracted rate constants (**Figure S6**).

$$\text{Volmer Step: } i_{et} = nFAk^0 a_{H^+} \exp(-\alpha f \eta) \tag{24}$$

$$\text{Heyrovsky Step: } i_{et} = nFA \frac{k^0 K^0 a_{H^+}^2 \exp(-\alpha f \eta)}{\exp(f\eta) + K^0 a_{H^+}} \tag{25}$$

$$\text{Tafel Step: } i_{et} = nFAk^0 \left[\frac{K^0 a_{H^+}^2}{\exp(f\eta) + K^0 a_{H^+}} \right]^2 \tag{26}$$

We conducted nonlinear regression using both Heyrovsky and Tafel models to fit the experimental data. As shown in **Figure 14a–b**, the Heyrovsky model fits most data points well, (R^2 = 0.9407) but the Tafel model (R^2 = 0.7802) provides superior agreement at low overpotentials (0 V to –0.2 V vs Ag/AgCl), where surface hydrogen coverage is likely highest (**Figure 14b**). Accordingly, we adopted a mixed fitting approach: the low-overpotential region was first fitted with the Tafel model, and the residual current (after subtracting the Tafel contribution) was subsequently fitted with the Heyrovsky model.(R^2 = 0.7802) This combined model captures the potential range up to –0.5 V and highlights a transition of the RDS from the Tafel step to the Heyrovsky step as overpotential increases (**Figure 14c–d**). It also gives us the best fitting level, with R^2 = 0.9954, after the two red points were excluded. The extracted kinetic parameters for the Heyrovsky-only, Tafel-only, and combined fitting procedures are summarized in **Table 1**.

Table 1: Extracted kinetic parameters from nonlinear fitting of HER models on citrate-capped Pd NPs.

Fitting Model	k^0 **(m/s)**	K^0 **(mM^{-1})**	α
Heyrovsky-only	6.63×10^{-7}	1.275×10^{-5}	0.059
Tafel-only	9.634×10^{-5}	1.546×10^{-5}	–
Tafel + Heyrovsky: Tafel component	1.671×10^{-5}	4.962×10^{-4}	–
Tafel + Heyrovsky:Heyrovsky component	7.661×10^{-9}	2.807×10^{-5}	0.290

According to **Table 1** and **Figure 14**, we found that if the reaction proceeds solely through the Heyrovsky pathway, the extracted standard rate constant (k^0) on Pd NPs is only about 1% of that reported for Pt NP collisions. The equilibrium constant for hydrogen adsorption/absorption is also extremely small. Furthermore, the transfer coefficient is anomalously low (α = 0.059), indicating that only a small fraction of the applied overpotential is effectively utilized to drive the charge transfer across the activation barrier. Since the charge transfer coefficient (α) signifies the portion of the electric field that contributes to promoting the reaction coordinate over the free energy barrier, such a low value suggests that even large overpotentials do little to accelerate the reaction. Collectively, these results imply that the Heyrovsky step is unlikely to be rate-determining under the investigated conditions.

After excluding the influence of a potential Tafel component—which appeared constant over the potential range starting at $\eta = -0.2$ V—the extracted transfer coefficient (α) increased to 0.29, within the expected range of 0.3–0.7. Despite this improvement, the value remains closer to 0, suggesting that adsorbed hydrogen is more likely to become trapped within the Pd nanoparticle than undergo electrochemical desorption via the Heyrovsky step. Although the extracted standard rate constant (k^0) for the Heyrovsky step is several orders of magnitude smaller than that of the Tafel step, the Tafel pathway contributes much less to the total current at higher overpotentials. This apparent contradiction can be rationalized by the higher potential dependence of Heyrovsky step, but any higher overpotential, the Heyrovsky reactivity is likely deactivated by the increasing amount of hydride formed near or on the surface of Pd NP. Finally, the current stopped increasing exponentially following a kinetic control.

A comparison with Pt NPs further supports this conclusion. Defnet et al. reported $k^0 = 2.58 \times 10^{-3}$ m/s and $\alpha = 0.77$ for Pt, while other studies have also found significantly higher kinetic parameters for both Pt and Pd compared to the citrate-capped Pd NPs used here.[16, 37] These differences highlight Pt's superior HER activity and suggest that Volmer adsorption on Pd is thermodynamically and kinetically less favorable, possibly due to the competing tendency of Pd to absorb hydrogen into its bulk.

3.3.4 Hydrogen Absorption vs. Evolution

To place our single-entity results in a broader electrochemical context, we compared the hydrogen absorption behavior observed in our study with literature reports on ensemble Pd systems. The observed hydrogen absorption levels ($x \approx 0.08$–0.134) are significantly lower than those reported in a recent study using continuous Pd/C catalyst layers under RDE and proton pump configurations, where hydrogen fractions as high as $x \approx 0.47$ were achieved at only –0.2 V vs. RHE [73], not to say the extreme cases observed in faceted Pd NPs, where x values approaching 0.90 have been reached under low overpotentials and well-controlled conditions [10]. This contrast reveals the critical role of platform, surface structure, and experimental configuration in determining the extent of hydrogen uptake, and highlights the limitations of transient single-particle collision techniques in reaching absorption equilibrium.

By contrast, in our system, hydrogen absorption on single Pd NPs requires far more negative potentials (e.g., –1.0 V vs. Ag/AgCl) to reach even $x \approx 0.14$. Here, we provide several possible reasons for this key observation. One of them is that the Pd NPs used by Moumaneix *et al.* were only 3.8 nm in diameter, which falls within the size range where significant modifications of the d-band structure and surface electronic states are known to occur. When the size of the NPs decreases, their d-band center tends to move upward, closer to the Fermi level.[79] Then, the hydrogen solution energy decreases, leading to a stronger Pd–H bond and thus a higher hydrogen absorption ability.[80] Therefore, the hydrogen absorption efficiency of our 56 nm Pd NP is much lower than their 3.8 nm NP.

Moreover, similar contrasts are observed when comparing with the highly faceted octahedral Pd NPs studied by Zalineeva *et al.*, which exhibited hydrogen fractions as high as $x = 0.90$ under much milder conditions.[10] Their system differs from ours in 2 important ways: (1) highly crystalline, shape-controlled Pd nanocrystals exposing primarily $\{111\}$ facets that favor hydrogen uptake; and (2) much smaller particle sizes (ca. 7.8 nm), enabling more efficient lattice relaxation during phase transitions. In contrast, our collision-based system is inherently transient and limited to sub-millisecond timescales, during which hydrogen absorption is kinetically restricted. Furthermore, the larger and less defined Pd NPs used in our study likely possess mixed or defected surface terminations, which further hinders rapid and deep hydrogen incorporation.

Similarly, we can use this reasoning to explain the significantly enhanced HER kinetics observed on the Pd-deposited CFE. After 15 cycles of electrodeposition, the amount of Pd on the electrode surface can be considered bulk-like, with an electronic structure resembling that of extended polycrystalline Pd. Our Tafel analysis yielded a transfer coefficient of $\alpha = 0.43$ for the Pd-modified CFE—substantially higher than the values obtained from single Pd NP collisions, where α ranged from 0.06 to 0.29 depending on the fitted mechanism. According to the d-band model, a deeper d-band center in bulk Pd results in weaker hydrogen binding, which facilitates the desorption of hydrogen atoms and promotes the Heyrovsky or Tafel steps of HER. In contrast, single Pd NPs exhibit an upshifted d-band center, leading to stronger hydrogen adsorption and increased tendency for hydrogen absorption into the lattice rather than surface evolution. This fundamental difference in electronic structure explains the enhanced HER kinetics on the bulk-like Pd electrode and the suppressed HER efficiency observed in single-NP collision experiments.

3.3.5 Collision Frequency

To investigate the relationship between acid concentration and NP collision frequency, we designed a set of experimental systems with matched total ionic strength. One set contained only perchloric acid ($HClO_4$) as the electrolyte at varying concentrations (1, 3, 10, and 25 mM), while the other set maintained a constant $HClO_4$ concentration at 1 mM and incrementally increased the concentration of inert salt $NaClO_4$ (0, 2, 9, and 24 mM) to match the total ionic strength of the corresponding acid-only systems.

The results showed that increasing acid concentration significantly enhanced the observed NP collision frequency and the associated current signal intensity. This indicates that elevated proton concentrations greatly promote the interfacial electrochemical kinetics of the HER during NP collisions, thereby improving signal detectability. However, we also observed that at higher acid concentrations, the collision frequency became much more variable, possibly due to NP aggregation induced by the high proton content. In contrast, systems with constant acid concentration and increased $NaClO_4$ did not exhibit any substantial increase in collision frequency. This suggests that simply increasing the ionic strength is insufficient to enhance the electrochemical response or the detectability of NP collisions.

In summary, acid concentration is the determining factor in regulating NP collision behavior. It not only supplies protons required for the HER but also directly influences interfacial reaction rates and current signal strength, thereby affecting both the detectability and stability of collision events. While ionic strength can modulate the electrical environment of the system, its effect is limited in the absence of electrochemically active species such as protons.

Additionally, under low acid conditions, collisions of smaller NPs often generate extremely weak current signals that may fall below the background noise threshold and thus go undetected. This further supports the idea that acid

concentration not only governs the availability of protons for HER but also determines whether individual collision events can be recorded.

We also performed Pd NP collision experiments using a gold UME. Despite the difference in electrode size, the observed collision frequency did not scale linearly with electrode radius,(**Figure 16**) inconsistent with previous reports.[34] This suggests that NP collisions by diffusion are fundamentally stochastic in nature. While empirical relationships have been proposed to describe collision frequency, our results indicate that it is challenging to extract quantitative information solely based on frequency data.

3.3.6 Error Analysis

We recognize that other processes may contribute to the charge analyzed above. The first is double-layer charging, which arises from the redistribution of electrolyte ions at the NP–electrode interface upon potential contact. Based on literature-reported capacitance values for low-index Pd surfaces,[81] the estimated charge associated with a 56 nm spherical Pd NP undergoing a 0.7 V potential step is approximately 2.2 fC for Pd(111), 2.6 fC for Pd(100), and 4.5 fC for Pd(110). These values represent the upper bound of non-faradaic charging and provide a quantitative baseline for evaluating the total measured collision charge.

The second possible contribution is from the oxygen reduction reaction (ORR). While ORR can, in principle, generate faradaic current during NP collisions, its influence is negligible under our experimental conditions. The applied potentials are substantially more negative than the typical ORR onset on Pd, and the electrolyte was purged with nitrogen to eliminate dissolved oxygen. Moreover, the observed charge is far below the theoretical diffusion-limited ORR estimate, indicating that oxygen reduction is unlikely to play a significant role.

The third possibility is hydrogen spillover. Although the extent of hydrogen spillover is difficult to quantify, we consider its contribution negligible in our system. The carbon fiber electrode (CFE) is chemically inert and lacks oxygen-containing functional groups—such as carboxylic acids—that are known to facilitate proton–electron pair migration from Pd surfaces.[82] Furthermore, perchloric acid does not oxidize or modify the CFE surface to introduce such anchoring sites. While our Pd NPs are stabilized by surface-bound citrate, this ligand is confined to the NP surface and does not form a bridge to the CFE or act as an effective acceptor for migrating hydrogen. Therefore, even if transient hydrogen adsorption occurs on the Pd surface, it is unlikely to transfer to the electrode or contribute significantly to the detected signal.

Taken together, these considerations suggest that double-layer charging is the only non-faradaic process that could

contribute meaningfully to the observed charge. However, even under the most favorable assumptions, its contribution accounts for no more than 3–5% of the total signal, and is thus insufficient to alter the conclusions presented here.

If we examine the figures plotting charge transfer more closely, we notice that the associated error bars are considerably wide. However, this variability is expected and scientifically justifiable. First, the Pd NPs used in our experiments are not highly monodisperse, and the size distribution is intrinsically broad. Since both adsorption and absorption charges scale with particle size, this directly contributes to the spread in measured values. Second, it has been shown that hydrogen absorption occurs on Pd NPs.(**Figure S7**) However, the extent of absorption varies between particles due to differences in hydrogen absorption kinetics and internal diffusion limitations, further widening the distribution of experimental charges. Third, single-NP collisions are inherently stochastic processes. Variations in contact geometry, duration, and local electrochemical environment introduce additional randomness into the observed signals, even for NPs of similar size and composition. Therefore, the observed charge values should not be interpreted as representing the behavior of any single NP, but rather as statistically averaged outcomes across a large number of independent collision events. While individual events may deviate significantly, the ensemble data provide meaningful insight into the dominant charge transfer mechanisms at play.

3.4 Outlook

While this study provides mechanistic insights into hydrogen adsorption and evolution on single Pd NPs through collision electrochemistry, several directions remain open for further exploration. One important goal is to enhance the efficiency and selectivity of hydrogen absorption and evolution during NP collisions. This may be achieved by tuning the electrolyte composition, modifying the electrode interface, or engineering the surface structure of the NPs to lower kinetic barriers. Notably, Namba et al. demonstrated that submonolayer alloying of Pd(110) with Au can accelerate hydrogen absorption by over 40-fold, by destabilizing surface-adsorbed hydrogen and promoting subsurface penetration.[83] Such surface-engineering strategies may inspire future designs of alloyed or facet-controlled Pd NPs with tailored absorption behavior.

Another promising direction is the synthesis of more monodisperse Pd NPs. Reducing particle size heterogeneity would directly narrow the distribution of charge signals and enable more precise quantitative analysis of single-particle behavior. Advanced colloidal methods or post-synthetic sorting strategies (e.g., size-selective centrifugation) could be employed to improve size uniformity. This could also facilitate the size-dependence study. But it should be pointed out that smaller NPs may exhibit higher absorption efficiency and collision efficiency, but at the same time they tends to give smaller signals that is easily submerged in the overwhelming background noise. In addition, coupling

single-NP collision electrochemistry with complementary spectroscopic techniques—such as surface-enhanced Raman spectroscopy (SERS)—may provide direct evidence for Pd–H bond formation, offering molecular-level validation of hydrogen absorption processes. Such operando spectroelectrochemical approaches could reveal transient surface and lattice states during the collision process. Finally, here we are still unable to discriminate hydrogen adsorption and absorption very well, given that H diffuses in Pd very fast. Techniques and instruments with higher temporal resolution is required to accomplish this.

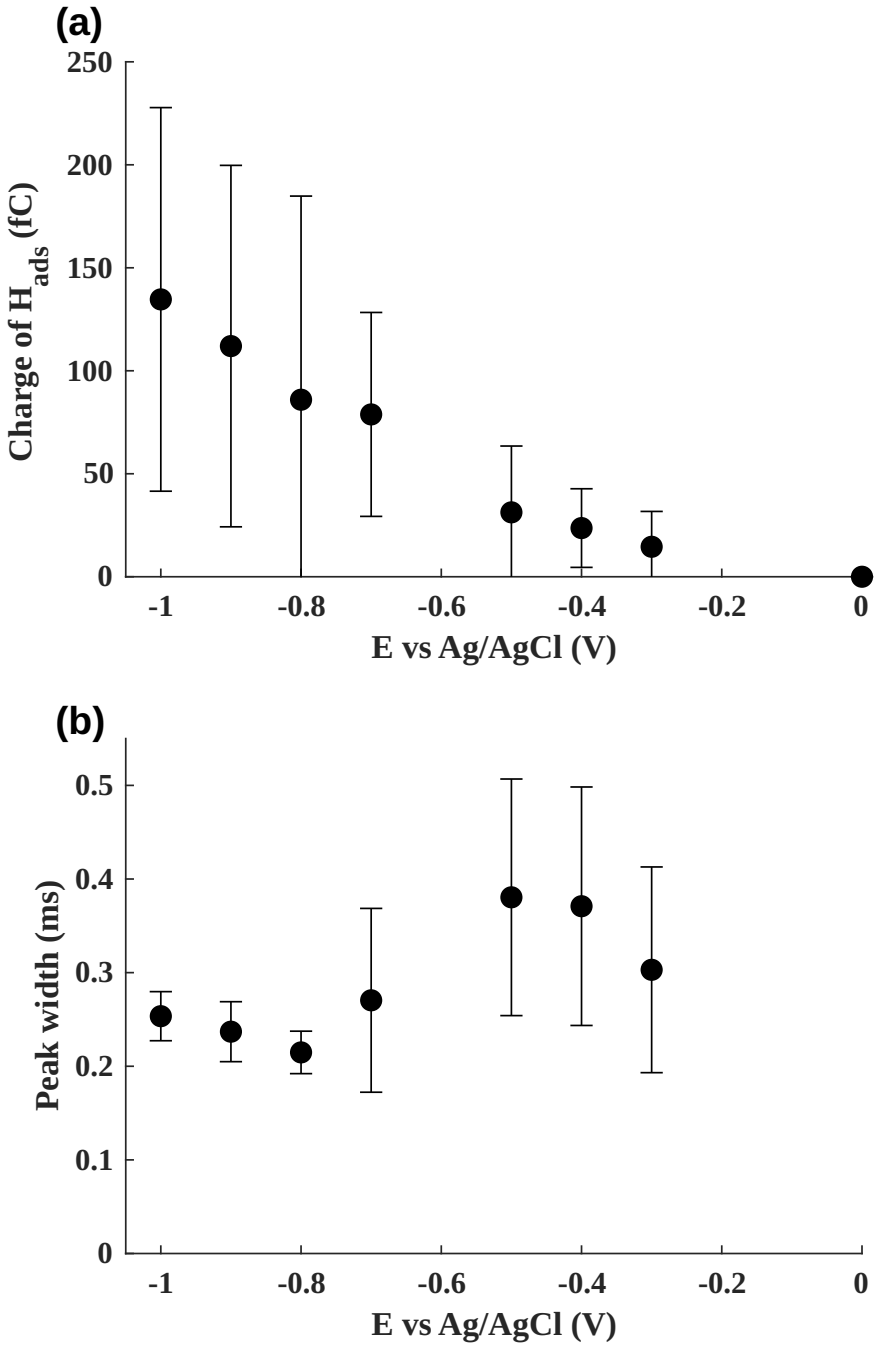

Figure 13: (a) Total charge associated with adsorbed hydrogen increases with more negative applied potential vs. Ag/AgCl, indicating more complete surface coverage or partial hydrogen absorption at higher overpotential. (b) Peak width fluctuating with applied potential from 0V vs. Ag/AgCl. Chronoaperograms were recorded in a 25 mM $HClO_4$ solution with 60 uL Pd NP solution added.

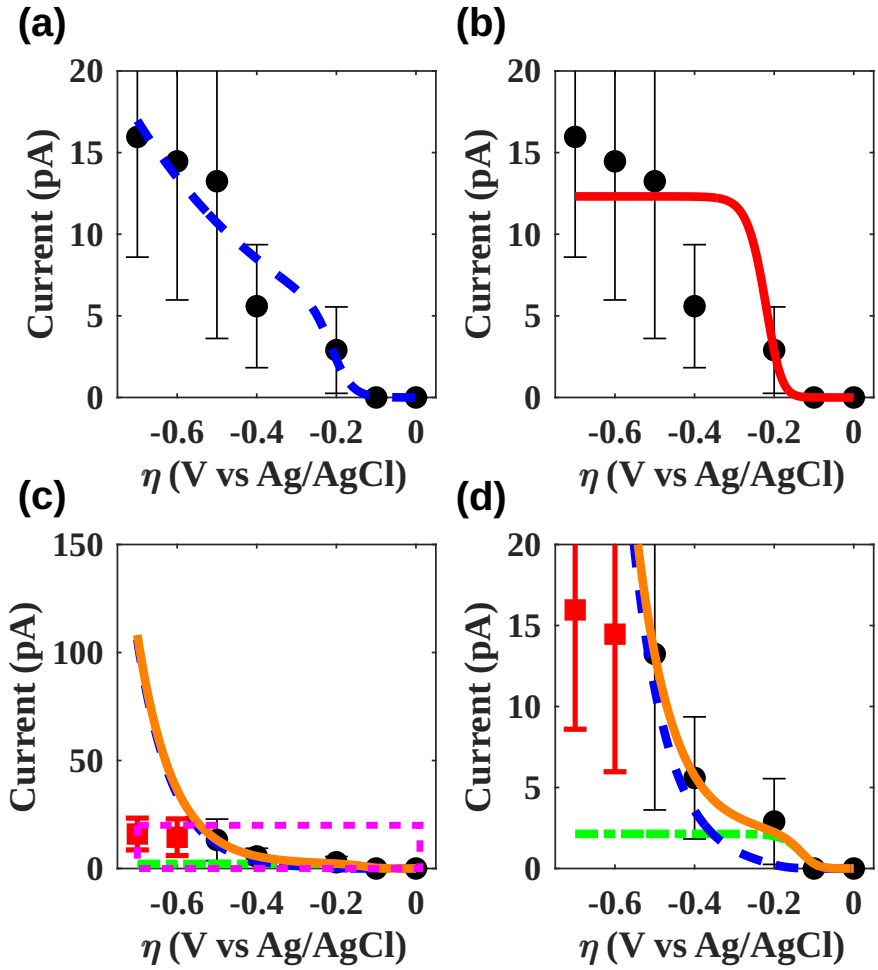

Figure 14: (a) Heyrovsky model fitting (blue dashed line) to full experimental data (black circles with error bars) using all measured current values. (b) Tafel model fitting (red solid line) to the same full data, showing a sigmoidal shape due to the Langmuir-type adsorption component. (c) Tafel fitting (green dashed line), Heyrovsky (blue dashed line), and combined fitting (orange solid line) to a truncated dataset (black circles); excluded data points (red squares) are not included in the fitting. Magenta dashed rectangle region was zoomed in in (d). Each model curve is computed from the optimized parameters obtained via nonlinear least-squares fitting. The fitted curves illustrate the contributions of surface adsorption (Tafel step) and electrochemical desorption (Heyrovsky step) to the overall current.

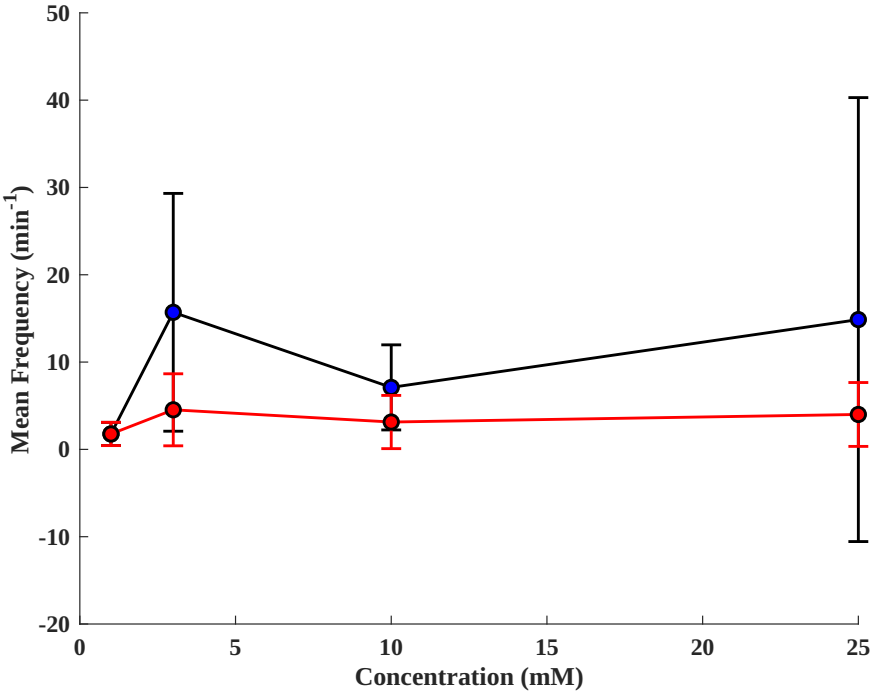

Figure 15: Comparison of mean event frequencies under varying acid concentrations and at 1 mM acid with different concentration of additional $NaClO_4$ to reach the same total concentration with the acid. Blue markers represent the condition with acid only (e.g., $HClO_4$), while red markers indicate the presence of $NaClO_4$ to compensate the electrolyte concentration. Error bars represent standard deviations. All experiments were done at -700 mV vs. Ag/AgCl and with the same NP concentration.

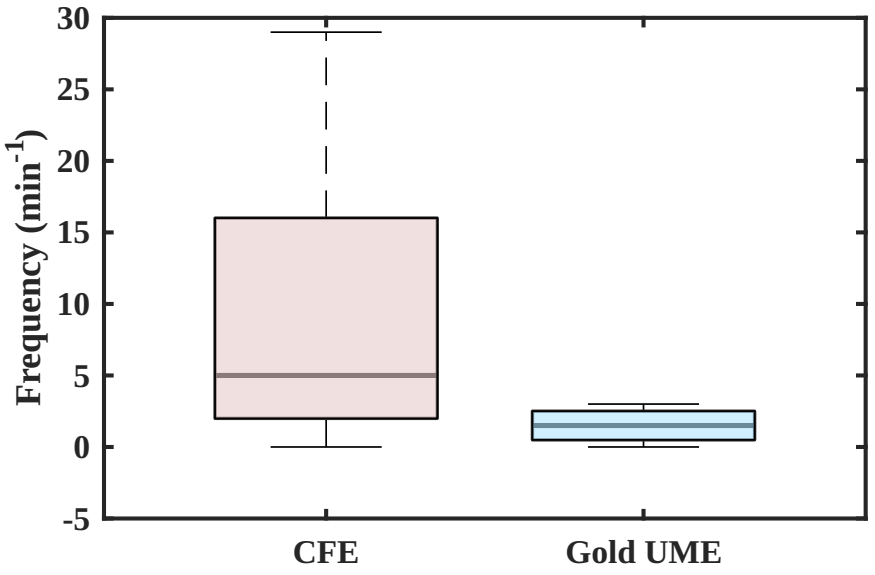

Figure 16: Collision frequency of Pd NP with 5 μm CFE (red) and 25 μm Au UME, with 60 μL Pd NP and 25 mM $HClO_4$.

4 Conclusion

Here, we present a comprehensive investigation of the hydrogen evolution reaction (HER) kinetics and hydrogen absorption on single palladium nanoparticles (Pd NPs) using stochastic collision experiments. Through systematic analysis of current transients, we reveal that Pd NPs undergo both surface hydrogen adsorption and bulk absorption, leading to the formation of palladium hydride (PdH_x) during HER. By comparing the kinetics on bulk Pd and single Pd NPs, we find that hydrogen absorption is more efficient on Pd NPs, whereas HER is less efficient. Notably, our findings demonstrate that hydrogen absorption significantly impedes hydrogen evolution by limiting the fraction of adsorbed hydrogen that recombines to form H_2. By evaluating the effects of proton concentration and applied potential, we show that the HER process on Pd deviates from conventional Volmer–Heyrovsky or Volmer–Tafel mechanisms. Instead, the observed low transfer coefficients and apparent rate constants indicate a slow, absorption-dominated pathway. These insights underscore the critical role of hydrogen absorption kinetics in determining the electrocatalytic behavior of Pd at the nanoscale and establish single-NP collision as a powerful technique for disentangling complex reaction pathways in heterogeneous catalysis.

References

[1] Thanh Tuan Le, Prabhakar Sharma, Bhaskor Jyoti Bora, Viet Dung Tran, Thanh Hai Truong, Huu Cuong Le, and Phuoc Quy Phong Nguyen. Fueling the future: A comprehensive review of hydrogen energy systems and their challenges. *International Journal of Hydrogen Energy*, 54:791–816, 2024.

[2] Center for Sustainable Systems, University of Michigan. Hydrogen factsheet, 2024. Pub. No. CSS23-07.

[3] Pedro J. Megía, Arturo J. Vizcaíno, José A. Calles, and Alicia Carrero. Hydrogen production technologies: From fossil fuels toward renewable sources. a mini review. *Energy & Fuels*, 35(20):16403–16415, 2021.

[4] Muhammad R. Usman. Hydrogen storage methods: Review and current status. *Renewable and Sustainable Energy Reviews*, 167:112743, 2022.

[5] G. Li, H. Kobayashi, J. Taylor, et al. Hydrogen storage in pd nanocrystals covered with a metal–organic framework. *Nature Materials*, 13:802–806, August 2014. Published: 13 July 2014, Received: 25 January 2014, Accepted: 09 May 2014.

[6] T. Yakabe, G. Imamura, G. Yoshikawa, and et al. 2-step reaction kinetics for hydrogen absorption into bulk material via dissociative adsorption on the surface. *Scientific Reports*, 11:18836, 2021. Published online: 22 September 2021.

[7] K. Hubkowska, M. Pajak, D. Monikowska, et al. Pd–h as an irreplaceable model system for the study of hydrogen electrosorption in aqueous and non-aqueous electrolytes. *Journal of Solid State Electrochemistry*, 28:1159–1169, 2024. Published online: 19 January 2024.

[8] Michael Schwarzer, Nils Hertl, Florian Nitz, Dmitriy Borodin, Jan Fingerhut, Theofanis N. Kitsopoulos, and Alec M. Wodtke. Adsorption and absorption energies of hydrogen with palladium. *The Journal of Physical Chemistry C*, 126(34):14500–14508, 2022.

[9] Emil Roduner. Size matters: why nanomaterials are different. *Chemical Society Reviews*, 35:583–592, 2006.

[10] Anna Zalineeva, Stève Baranton, Christophe Coutanceau, and Gregory Jerkiewicz. Octahedral palladium nanoparticles as excellent hosts for electrochemically adsorbed and absorbed hydrogen. *Science Advances*, 3(2):e1600542, 2017.

[11] Denys S. Butenko, Shilin Li, Volodymyr O. Kotsyubynsky, Volodymyra M. Boychuk, Volodymyr I. Dubinko, Pavlo I. Kolkovsky, Nikita A. Liedienov, N.I. Klyui, Wei Han, and Igor V. Zatovsky. Palladium nanoparticles embedded in microporous carbon as electrocatalysts for water splitting in alkaline media. *International Journal of Hydrogen Energy*, 46(41):21462–21474, 2021.

[12] Mehtap Aygün, Melanie Guillen-Soler, Jose M. Vila-Fungueiriño, Abdullah Kurtoglu, Thomas W. Chamberlain, Andrei N. Khlobystov, and Maria del Carmen Gimenez-Lopez. Palladium nanoparticles hardwired in carbon nanoreactors enable continually increasing electrocatalytic activity during the hydrogen evolution reaction. *ChemSusChem*, 14(22):4973–4984, 2021.

[13] Tatsuya Shinagawa, Angel T. Garcia-Esparza, and Kazuhiro Takanabe. Insight on tafel slopes from a microkinetic analysis of aqueous electrocatalysis for energy conversion. *Scientific Reports*, 5:13801, 2015.

[14] Onno van der Heijden, Sunghak Park, Rafaël E. Vos, Jordy J. J. Eggebeen, and Marc T. M. Koper. Tafel slope plot as a tool to analyze electrocatalytic reactions. *ACS Energy Letters*, 9(4):1871–1879, 2024.

[15] Chengzhang Wan, Yansong Ling, Sibo Wang, Heting Pu, Yu Huang, and Xiangfeng Duan. Unraveling and resolving the inconsistencies in tafel analysis for hydrogen evolution reactions. *ACS Central Science*, 10(3):658–665, 2024.

[16] Shima Haghighat and Jahan M. Dawlaty. ph dependence of the electron-transfer coefficient: Comparing a model to experiment for hydrogen evolution reaction. *The Journal of Physical Chemistry C*, 120(50):28489–28496, 2016.

[17] Zhi-peng Xiang, Hai-qiang Deng, Pekka Peljo, Zhi-yong Fu, Su-li Wang, Daniel Mandler, Gong-quan Sun, and Zhen-xing Liang. Electrochemical dynamics of a single platinum nanoparticle collision event for the hydrogen evolution reaction. *Angewandte Chemie International Edition*, 57(13):3464–3468, 2018.

[18] Peter A. Defnet and Bo Zhang. Detection of transient nanoparticle collision events using electrochemiluminescence on a closed bipolar microelectrode. *ChemElectroChem*, 7(1):252–259, 2020.

[19] Aleksandar R. Zeradjanin, George Polymeros, Cigdem Toparli, Marc Ledendecker, Nejc Hodnik, Andreas Erbe, Michael Rohwerder, and Fabio La Mantia. What is the trigger for the hydrogen evolution reaction? – towards electrocatalysis beyond the sabatier principle. *Phys. Chem. Chem. Phys.*, 22:8768–8780, 2020.

[20] Allen J. Bard and Larry R. Faulkner. *Electrochemical Methods: Fundamentals and Applications*. Wiley, 2nd edition, 2001.

[21] Paul Sabatier. *La catalyse en chimie organique*. Librairie Polytechnique, Paris et Liège, 1920.

[22] A A Balandin. Modern state of the multiplet theory of heterogeneous catalysis. *Advances in catalysis*, 19:1–210, 1969.

[23] Sergio Trasatti. Work function, electronegativity, and electrochemical behaviour of metals: Iii. electrolytic hydrogen evolution in acid solutions. *Journal of Electroanalytical Chemistry and Interfacial Electrochemistry*, 39(1):163–184, 1972.

[24] Jens Kehlet Nørskov, Thomas Bligaard, Ashildur Logadottir, J.R. Kitchin, J.G. Chen, S. Pandelov, and U. Stimming. Trends in the exchange current for hydrogen evolution. *Journal of The Electrochemical Society*, 152(2):J23–J26, 2005. Copyright The Electrochemical Society, Inc. [2005]. All rights reserved. Except as provided under U.S. copyright law, this work may not be reproduced, resold, distributed, or modified without the express permission of The Electrochemical Society (ECS).

[25] Paola Quaino, Fernanda Juarez, Elizabeth Santos, and Wolfgang Schmickler. Volcano plots in hydrogen electrocatalysis – uses and abuses. *Beilstein Journal of Nanotechnology*, 5:846–854, 2014.

[26] M. Lukaszewski, M. Soszko, and A. Czerwiński. Electrochemical methods of real surface area determination of noble metal electrodes – an overview. *International Journal of Electrochemical Science*, 11(6):4442–4469, 2016.

[27] F. D. Manchester, A. San-Martin, and J. M. Pitre. The h-pd (hydrogen-palladium) system. *Journal of Phase Equilibria*, 15(1):62–83, 1994.

[28] Ying Chen, Yucheng Hou, Gennady Govor, Olga Demidenko, and Yujing Li. Hydrogen absorption in palladium-based nanocrystals for electrocatalysis investigation. *ChemElectroChem*, 11(12):e202400071, 2024.

[29] T. Narayan, F. Hayee, A. Baldi, and et al. Direct visualization of hydrogen absorption dynamics in individual palladium nanoparticles. *Nature Communications*, 8:14020, 2017. Published online: 16 January 2017.

[30] Bernadette M. Quinn, Pieter G. van't Hof, and Serge G. Lemay. Time-resolved electrochemical detection of discrete adsorption events. *Journal of the American Chemical Society*, 126(27):8360–8361, 2004. PMID: 15237976.

[31] Xiaoyin Xiao and Allen J Bard. Observing single nanoparticle collisions at an ultramicroelectrode by electrocatalytic amplification. *J Am Chem Soc*, 129(31):9610–9612, July 2007.

[32] Xiaoyin Xiao, Fu-Ren F Fan, Jiping Zhou, and Allen J Bard. Current transients in single nanoparticle collision events. *J Am Chem Soc*, 130(49):16669–16677, December 2008.

[33] Seong Jung Kwon, Fu-Ren F. Fan, and Allen J. Bard. Observing iridium oxide (irox) single nanoparticle collisions at ultramicroelectrodes. *Journal of the American Chemical Society*, 132(38):13165–13167, 2010. PMID: 20809574.

[34] Seong Jung Kwon, Hongjun Zhou, Fu-Ren F. Fan, Vasily Vorobyev, Bo Zhang, and Allen J. Bard. Stochastic electrochemistry with electrocatalytic nanoparticles at inert ultramicroelectrodes—theory and experiments. *Phys. Chem. Chem. Phys.*, 13:5394–5402, 2011.

[35] Juhan M. Kahk, Neil V. Rees, Jeseelan Pillay, Robert Tshikhudo, Sibulelo Vilakazi, and Richard G. Compton. Electron transfer kinetics at single nanoparticles. *Nano Today*, 7(3):174–179, 2012.

[36] Todd J. Anderson and Bo Zhang. Single-nanoparticle electrochemistry through immobilization and collision. *Accounts of Chemical Research*, 49(11):2625–2631, 2016. PMID: 27730817.

[37] Peter A. Defnet, Chu Han, and Bo Zhang. Temporally-resolved ultrafast hydrogen adsorption and evolution on single platinum nanoparticles. *Analytical Chemistry*, 91(6):4023–4030, 2019. PMID: 30785269.

[38] Yi-Ge Zhou, Neil V. Rees, and Richard G. Compton. The electrochemical detection and characterization of silver nanoparticles in aqueous solution. *Angewandte Chemie International Edition*, 50(18):4219–4221, 2011.

[39] Yi-Ge Zhou, Neil V. Rees, and Richard G. Compton. Electrode–nanoparticle collisions: The measurement of the sticking coefficient of silver nanoparticles on a glassy carbon electrode. *Chemical Physics Letters*, 514(4):291–293, 2011.

[40] César A. Ortiz-Ledón and Cynthia G. Zoski. Pt nanoparticle collisions detected by electrocatalytic amplification and atomic force microscopy imaging: Nanoparticle collision frequency, adsorption, and random distribution at an ultramicroelectrode surface. *Analytical Chemistry*, 89(12):6424–6431, 2017. PMID: 28541030.

[41] Donald A. Robinson, Yuwen Liu, Martin A. Edwards, Nicholas J. Vitti, Stephen M. Oja, Bo Zhang, and Henry S. White. Collision dynamics during the electrooxidation of individual silver nanoparticles. *Journal of the American Chemical Society*, 139(46):16923–16931, 2017. PMID: 29083174.

[42] Linlin Sun, Wei Wang, and Hong-Yuan Chen. Dynamic nanoparticle-substrate contacts regulate multi-peak behavior of single silver nanoparticle collisions. *ChemElectroChem*, 5(20):2995–2999, 2018.

[43] Kim McKelvey, Donald A. Robinson, Nicholas J. Vitti, Martin A. Edwards, and Henry S. White. Single ag nanoparticle collisions within a dual-electrode micro-gap cell. *Faraday Discuss.*, 210:189–200, 2018.

[44] Huimin Ma, Jiafeng Chen, Haifeng Wang, and Peng Chen. Exploring dynamic interactions of single nanoparticles at interfaces for surface-confined electrochemical behavior and size measurement. *Nature Communications*, 11:2307, 2020.

[45] Yunfeng Xu, Wenjun Jiang, Yuyan Bai, Yujie Yang, and Zhilun Zhang. Artificial intelligence-assisted multi-parameter size discrimination of silver nanoparticles through electrochemical collision. *Analytical Chemistry*, 96(16):6195–6201, 2024.

[46] Rui Hao and Bo Zhang. Observing electrochemical dealloying by single-nanoparticle collision. *Analytical Chemistry*, 88(17):8728–8734, 2016. PMID: 27476812.

[47] Germano P. Santos, Antonio F. A. A. Melo, and Frank N. Crespilho. Magnetically controlled single-nanoparticle detection via particle–electrode collisions. *Phys. Chem. Chem. Phys.*, 16:8012–8018, 2014.

[48] Donald A. Robinson, Jason J. Yoo, Alma D. Castañeda, Brett Gu, Radhika Dasari, Richard M. Crooks, and Keith J. Stevenson. Increasing the collision rate of particle impact electroanalysis with magnetically guided pt-decorated iron oxide nanoparticles. *ACS Nano*, 9(7):7583–7595, 2015. PMID: 26168795.

[49] Jing Jiang, Xinjian Huang, and Lishi Wang. Effect of forced convection on the collision and interaction between nanoparticles and ultramicroelectrode. *Journal of Colloid and Interface Science*, 467:158–164, 2016.

[50] Qian Wang, Je Hyun Bae, Alexander B. Nepomnyashchii, Rui Jia, Suojiang Zhang, and Michael V. Mirkin. Light-controlled nanoparticle collision experiments. *The Journal of Physical Chemistry Letters*, 11(8):2972–2976, 2020. PMID: 32216279.

[51] Aliaksei Boika, Scott N. Thorgaard, and Allen J. Bard. Monitoring the electrophoretic migration and adsorption of single insulating nanoparticles at ultramicroelectrodes. *The Journal of Physical Chemistry B*, 117(16):4371–4380, 2013. PMID: 23092206.

[52] Cheng Ma, Wanwan Wu, Lingling Li, Shaojun Wu, Jianrong Zhang, Zixuan Chen, and Jun-Jie Zhu. Dynamically imaging collision electrochemistry of single electrochemiluminescence nano-emitters. *Chem. Sci.*, 9:6167–6175, 2018.

[53] Chang-Hui Chen, Emma R. Ravenhill, Dmitry Momotenko, Yang-Rae Kim, Stanley C. S. Lai, and Patrick R. Unwin. Impact of surface chemistry on nanoparticle–electrode interactions in the electrochemical detection of nanoparticle collisions. *Langmuir*, 31(43):11932–11942, 2015. PMID: 26448140.

[54] Alma D. Castañeda, Donald A. Robinson, Keith J. Stevenson, and Richard M. Crooks. Electrocatalytic amplification of dna-modified nanoparticle collisions via enzymatic digestion. *Chem. Sci.*, 7:6450–6457, 2016.

[55] Alma D. Castañeda, Timothy M. Alligrant, James A. Loussaert, and Richard M. Crooks. Electrocatalytic amplification of nanoparticle collisions at electrodes modified with polyelectrolyte multilayer films. *Langmuir*, 31(2):876–885, 2015. PMID: 25568965.

[56] Hyun S. Ahn and Allen J. Bard. Single-nanoparticle collision events: Tunneling electron transfer on a titanium dioxide passivated n-silicon electrode. *Angewandte Chemie International Edition*, 54(46):13753–13757, 2015.

[57] V. G. Artemov, E. Uykur, P. O. Kapralov, A. Kiselev, K. Stevenson, H. Ouerdane, and M. Dressel. Anomalously high proton conduction of interfacial water. *The Journal of Physical Chemistry Letters*, 11(9):3623–3628, 2020. PMID: 32329348.

[58] Seung Yeon Jung, Jin Woo Joo, and Seong Jung Kwon. Observation of blip response in a single pt nanoparticle collision on a cu ultramicroelectrode. *Bulletin of the Korean Chemical Society*, 37(3):349–354, 2016.

[59] Anahita Karimi, Silvana Andreescu, and Daniel Andreescu. Single-particle investigation of environmental redox processes of arsenic on cerium oxide nanoparticles by collision electrochemistry. *ACS Applied Materials & Interfaces*, 11(27):24725–24734, 2019. PMID: 31190542.

[60] Farideh Hosseini Narouei, Daniel Andreescu, and Silvana Andreescu. Rapid characterization of arsenic adsorption on single magnetite nanoparticles by collisions at microelectrodes. *Environ. Sci.: Nano*, 7:1999–2009, 2020.

[61] Abiola V. Oladeji, James M. Courtney, Marcos Fernandez-Villamarin, and Neil V. Rees. Electrochemical metal recycling: Recovery of palladium from solution and in situ fabrication of palladium-carbon catalysts via impact electrochemistry. *Journal of the American Chemical Society*, 144(40):18562–18574, 2022. PMID: 36179328.

[62] Naser Daryanavard and Hamid R. Zare. Single palladium nanoparticle collisions detection through chronopotentiometric method: Introducing a new approach to improve the analytical signals. *Analytical Chemistry*, 89(17):8901–8907, 2017. PMID: 28745042.

[63] June Young Park, Ki Jun Kim, Hyeryeon Son, and Seong Jung Kwon. Chronoamperometric observation and analysis of electrocatalytic ability of single pd nanoparticle for hydrogen peroxide reduction reaction. *Nanomaterials*, 8(11), 2018.

[64] Hubert Rudakemwa, Ki Jun Kim, Tae Eun Park, Hyeryeon Son, Jaedo Na, and Seong Jung Kwon. Observation and analysis of staircase response of single palladium nanoparticle collision on gold ultramicroelectrodes. *Nanomaterials*, 12(18), 2022.

[65] Mengjie Chen, Si-Min Lu, Peng Yueyi, Zhifeng Ding, and Yi-Tao Long. Tracking the electrocatalytic activity of a single palladium nanoparticle for the hydrogen evolution reaction. *Chemistry - A European Journal*, 27, 07 2021.

[66] Minkyung Kang, David Perry, Yang-Rae Kim, Alex W. Colburn, Robert A. Lazenby, and Patrick R. Unwin. Time-resolved detection and analysis of single nanoparticle electrocatalytic impacts. *Journal of the American Chemical Society*, 137(34):10902–10905, 2015. PMID: 26264494.

[67] Brian D. Adams and Aicheng Chen. The role of palladium in a hydrogen economy. *Materials Today*, 14(6):282–289, 2011.

[68] Seungyoung Park, Ki Jun Kim, and Seong Jung Kwon. Investigation of electrocatalytic activity of palladium nanoparticle for ammonia borane oxidation via single-entity electrochemistry. *Bulletin of the Korean Chemical Society*, 45(1):81–88, 2024.

[69] Milad Rezaei, Seyed Hadi Tabaian, and Davoud Fatmehsari Haghshenas. Electrochemical nucleation of palladium on graphene: A kinetic study with an emphasis on hydrogen co-reduction. *Electrochimica Acta*, 87:381–387, 2013.

[70] Adrian S. Bravo-Rodriguez and et al. Palladium electrodeposition onto a carbon fiber ultramicroelectrode. *Croatica Chemica Acta*, 95(2):49–55, 2022. Natural Science Collection; Publicly Available Content Database.

[71] O.V. Belousov, Y.V. Saltykov, L.I. Dorokhova, L.A. Solov'ev, and S.M. Zharkov. The dependence of the pdcl^2 /pd electrode potential on the dispersity of metallic palladium. *Russ. J. Phys. Chem.*, 82(4):647–650, 2008. Published: 02 May 2014, Received: 07 February 2006, Issue Date: April 2008.

[72] Tong Zhang, Xun Zhu, Ding-Ding Ye, Rong Chen, Yuan Zhou, and Qiang Liao. Cyclic voltammetry electrodeposition of well-dispersed pd nanoparticles on carbon paper as a flow-through anode for microfluidic direct formate fuel cells. *Nanoscale*, 12:20270–20278, 2020.

[73] Lilian Moumaneix, Akseli Rautakorpi, and Tanja Kallio. Interactions between hydrogen and palladium nanoparticles: Resolving adsorption and absorption contributions. *ChemElectroChem*, 10(6):e202201109, 2023.

[74] Xiaoting Chen, Laura P. Granda-Marulanda, Ian T. McCrum, and Marc T. M. Koper. Adsorption processes on a pd monolayer-modified pt(111) electrode. *Chem. Sci.*, 11:1703–1713, 2020.

[75] Hajime Kimizuka, Shigenobu Ogata, and Motoyuki Shiga. Mechanism of fast lattice diffusion of hydrogen in palladium: Interplay of quantum fluctuations and lattice strain. *Phys. Rev. B*, 97:014102, Jan 2018.

[76] Yang Li and Yang-Tse Cheng. Hydrogen diffusion and solubility in palladium thin films. *International Journal of Hydrogen Energy*, 21(4):281–291, 1996.

[77] Shun Dekura, Hiroshi Akiba, Osamu Yamamuro, Hirokazu Kobayashi, Mitsuhiko Maesato, and Hiroshi Kitagawa. New insights on the formation process and thermodynamics of the -phase pdh(d)x through direct enthalpy measurement of h(d) dissolution. *The Journal of Physical Chemistry C*, 124(16):8663–8668, 2020.

[78] Hector Prats and Karen Chan. The determination of the hor/her reaction mechanism from experimental kinetic data. *Phys. Chem. Chem. Phys.*, 23:27150–27158, 2021.

[79] Eishiro Toyoda, Ryosuke Jinnouchi, Tatsuya Hatanaka, Yu Morimoto, Kei Mitsuhara, Anton Visikovskiy, and Yoshiaki Kido. The d-band structure of pt nanoclusters correlated with the catalytic activity for an oxygen reduction reaction. *The Journal of Physical Chemistry C*, 115(43):21236–21240, 2011.

[80] Qisi Zhu, Weiwei Huang, Chao Huang, Lei Gao, Yanjing Su, and Lijie Qiao. The d band center as an indicator for the hydrogen solution and diffusion behaviors in transition metals. *International Journal of Hydrogen Energy*, 47(90):38445–38454, 2022.

[81] Elena Gubanova, Thorsten O. Schmidt, Sebastian Watzele, Vitaly Alexandrov, and Aliaksandr S. Bandarenka. Structure-dependent electrical double-layer capacitances of the basal plane pd(hkl) electrodes in hclo4. *The Journal of Physical Chemistry C*, 126(27):11414–11420, 2022.

[82] Javier Navarro-Ruiz, Jérémy Audevard, Mathieu Vidal, Cristian H. Campos, Iker Del Rosal, Philippe Serp, and Iann C. Gerber. Mechanism of hydrogen spillover on metal-doped carbon materials: Surface carboxylic groups are key. *ACS Catalysis*, 14(9):7111–7126, 2024.

[83] Kazuhiro Namba, Shohei Ogura, Satoshi Ohno, Wen Di, Koichi Kato, Markus Wilde, Ivo Pletikosić, Petar Pervan, Milorad Milun, and Katsuyuki Fukutani. Acceleration of hydrogen absorption by palladium through surface alloying with gold. *Proceedings of the National Academy of Sciences*, 115(31):7896–7900, 2018.

A Appendix A: Calculation of overpotential from applied potential

The conversion from Ag/AgCl to RHE is given by:

$$E_{\mathrm{RHE}} = E_{\mathrm{Ag/AgCl}} + 0.197\ \mathrm{V} + 0.0591 \times \mathrm{pH} \tag{27}$$

For measurements conducted in ultra-dilute perchloric acid (e.g., 0.1 mM $HClO_4$), the pH can be estimated as 4, which yields:

$$E_{\mathrm{RHE}} = E_{\mathrm{Ag/AgCl}} + 0.433\ \mathrm{V} \tag{28}$$

Since the standard potential of HER is 0 V vs. RHE, the overpotential can be calculated directly as:

$$\eta = E_{\mathrm{RHE}} - E^{\circ}_{\mathrm{HER}} = E_{\mathrm{RHE}} = E_{\mathrm{Ag/AgCl}} + 0.433\ \mathrm{V} \tag{29}$$

Similarly, for a 25 mM acid solution the overpotential was calculated as $E_{\mathrm{Ag/AgCl}} + 0.3$ V.

B Appendix B: Derivation of α and k^0 from Laviron Equation

We start with the Laviron equation:

$$E_p = E^0 + \frac{2.303RT}{\alpha nF} \log_{10}\left(\frac{RT}{\alpha nF} \cdot \frac{k^0}{v}\right) \tag{30}$$

Then, we separate the logarithm,

$$E_p = E^0 + \frac{2.303RT}{\alpha nF}\left[\log_{10}\left(\frac{RT}{\alpha nF}\right) + \log_{10}(k^0) - \log_{10}(v)\right] \tag{31}$$

This can be rewriten and reorganized into:

$$E_p = \frac{2.303RT}{\alpha nF}\log_{10}(v) + \left[E^0 + \frac{2.303RT}{\alpha nF}\log_{10}\left(\frac{RT}{\alpha nF} \cdot k^0\right)\right] \tag{32}$$

Thus,

$$\text{slope} = \frac{2.303RT}{\alpha nF} \tag{33}$$

and,

$$\text{intercept} = E^0 + \frac{2.303RT}{\alpha nF}\log_{10}\left(\frac{RT}{\alpha nF} \cdot k^0\right) \tag{34}$$

Therefore, we can obtain α and k^0 from the slope and intercept:

$$\alpha = \frac{2.303RT}{\text{slope} * nF} \tag{35}$$

and,

$$\log_{10}(k^0) = \log_{10}(v) + \frac{\alpha nF}{2.303RT}\left(-0.433V - \text{intercept}\right) \tag{36}$$

C Appendix C: Additional results of Pd electrodeposition

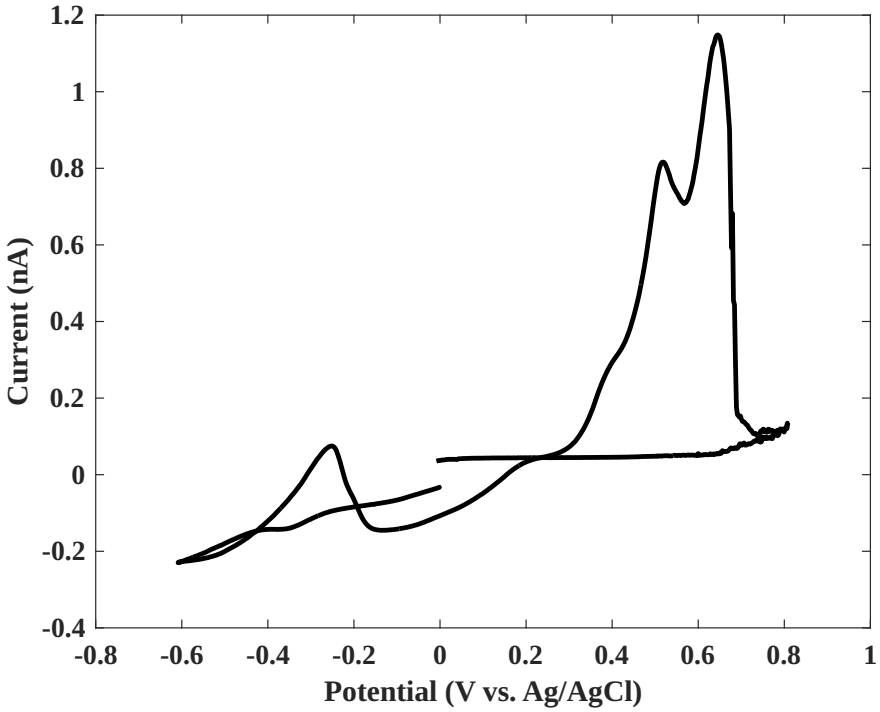

Figure S1: Additional Cyclic voltammogram of a Pd-modified microelectrode in 0.5 mM Pd(II) and 0.5 M supporting electrolyte, scanned from –0.6 V to +0.8 V vs. Ag/AgCl. In this attempt, the big anodic peak was split into a doublet,at +0.5 V and +0.6 V, which can be attributed to the oxidation of PdH_x and metallic Pd, respectively. The appearance of the doublet suggests the coexistence of multiple Pd species and potential hydride formation.

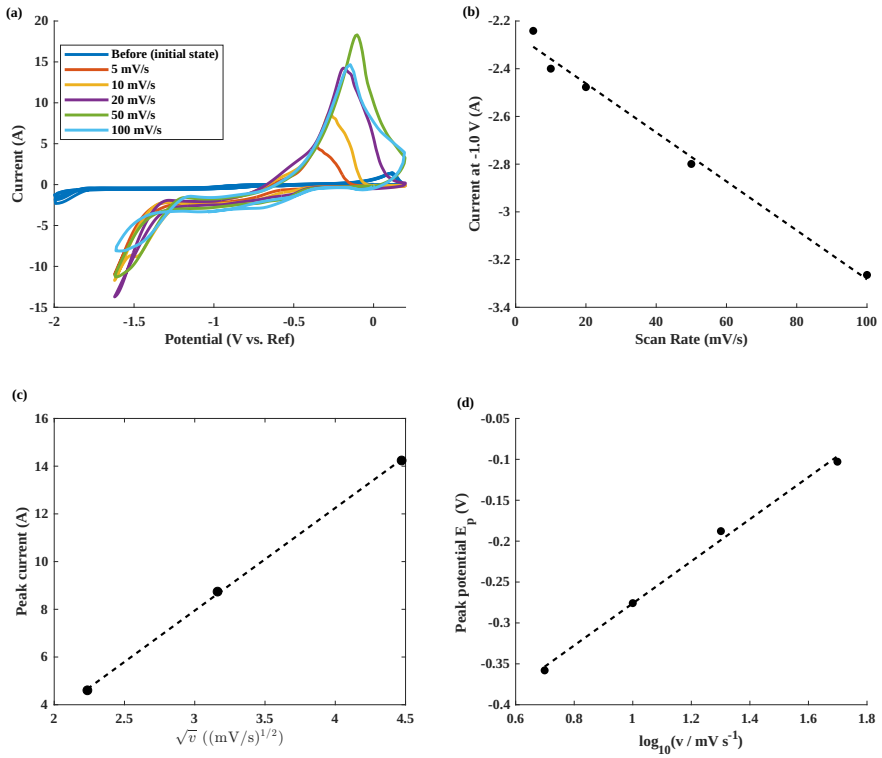

Figure S2: (a) Cyclic voltammograms of the system recorded at various scan rates ranging from 5 to 100 mV/s. (b) Plot of the current at –1.0 V versus scan rate with linear fitting (dashed line). (c) Peak current as a function of the square root of scan rate for scan rates of 5, 10, and 20 mV/s. (d) Laviron plot of peak potential versus log(scan rate) for 5, 10, 20, and 50 mV/s with linear fitting (dashed line).

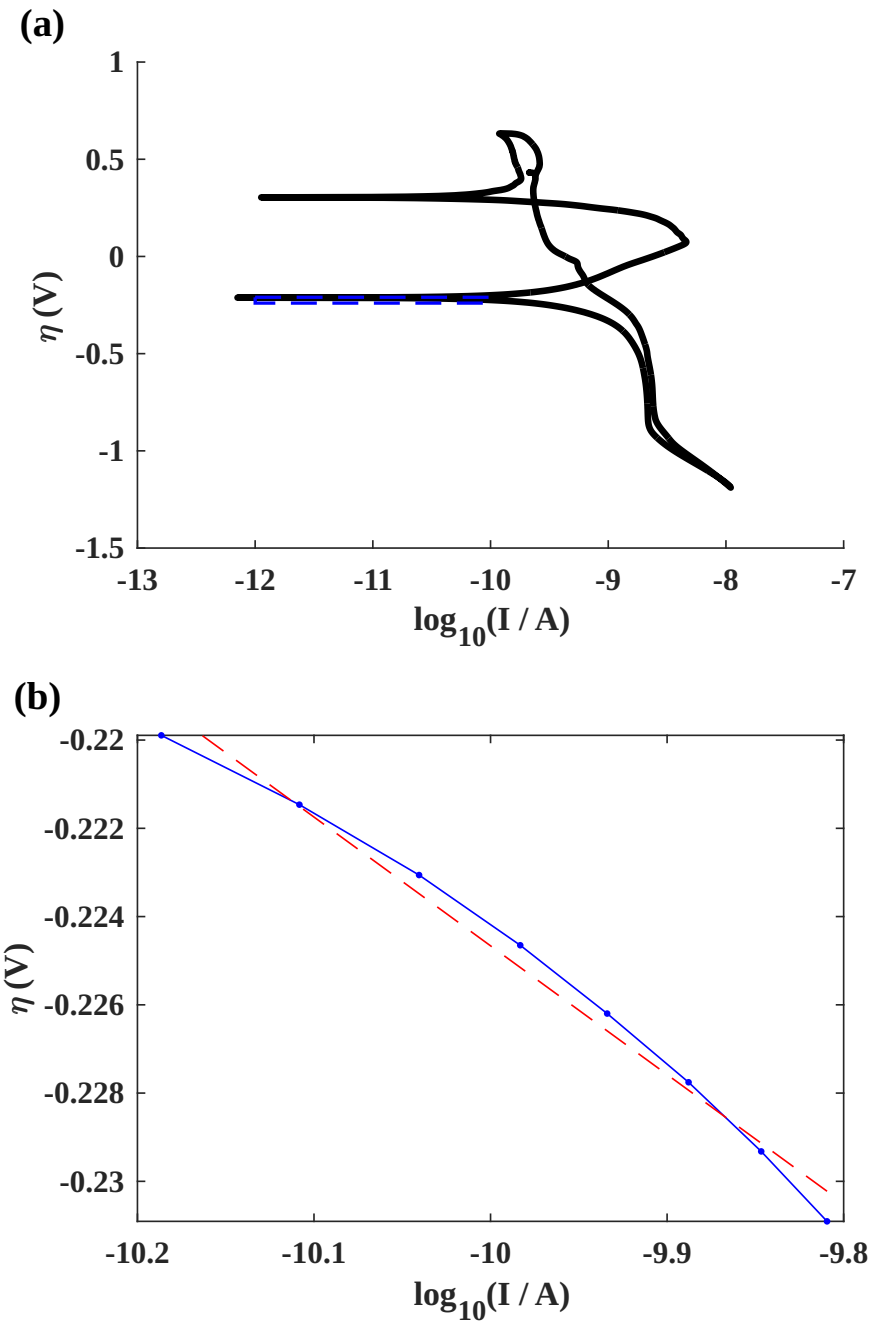

Figure S3: (a) Cyclic voltammogram of a Pd electrode in 0.1 mM $HClO_4$, plotted against $\log_{10}(I)$ to highlight the regions of potential Tafel behavior. The blue dashed line indicates the region selected for linear fitting. (b) Tafel plot of the selected region, showing the overpotential η as a function of $\log_{10}(I)$. The blue solid line represents the experimental data, and the red dashed line indicates the linear fit. A secondary y-axis shows the corresponding applied potential. The corelation coeffient is 0.9848.

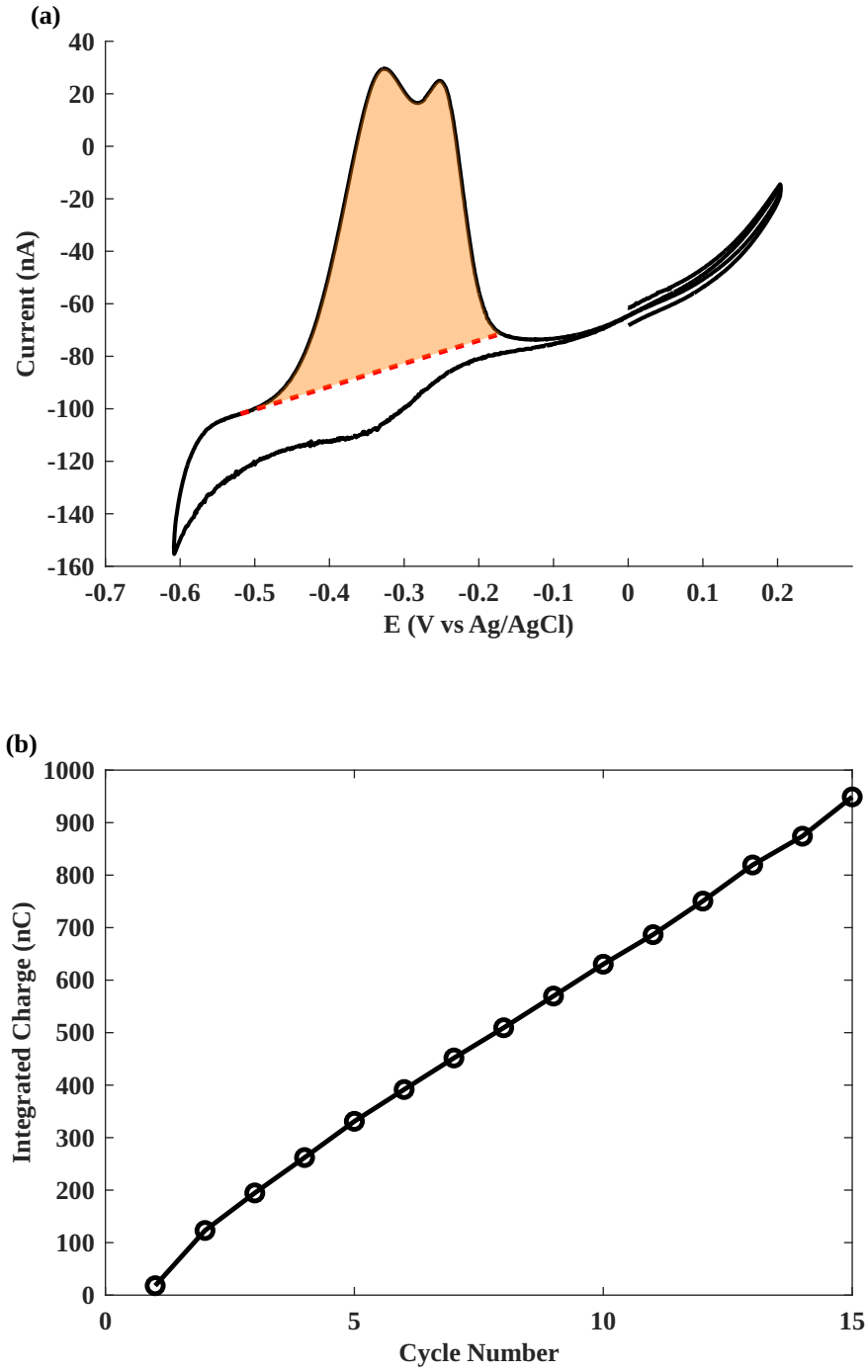

Figure S4: (a) Representative cyclic voltammogram (CV) during the 15th deposition cycle on a carbon fiber electrode (CFE), showing a pronounced anodic doublet near –0.2 V. The shaded region indicates the integrated charge associated with hydrogen desorption, with a linear baseline (dashed red) subtracted. (b) Plot of integrated anodic charge versus cycle number over 15 deposition cycles. The nearly linear increase in charge reflects the progressive growth of the electrochemically active Pd surface and volume.

D Appendix D: Calculation of Theoretical Time Resolution for a 2 kHz Low-Pass Filter

The temporal resolution of our electrochemical measurements is fundamentally limited by the characteristics of the low-pass filter applied during data acquisition. To evaluate the minimum resolvable timescale for transient features, we calculate the theoretical full width at half maximum (FWHM) imposed by the 2 kHz low-pass filter used in our experiments.

The characteristic rise time τ (defined as the time for the signal to increase from 10% to 90% of its final value) for a simple first-order low-pass filter is given by:

$$\tau = \frac{1}{2\pi f_c} \tag{37}$$

where f_c is the cutoff frequency of the filter.

Substituting $f_c = 2000$ Hz:

$$\tau = \frac{1}{2\pi \times 2000} \approx 7.96 \times 10^{-5}\,\text{s} = 79.6\,\mu\text{s} \tag{38}$$

For a Gaussian-shaped response, the full width at half maximum (FWHM) is related to the rise time by:

$$\text{FWHM} \approx 2.355 \times \tau \tag{39}$$

Thus, the theoretical FWHM corresponding to a 2 kHz low-pass filter is:

$$\text{FWHM} \approx 2.355 \times 79.6\,\mu\text{s} \approx 187\,\mu\text{s} = 0.187\,\text{ms} \tag{40}$$

This calculation indicates that any transient event narrower than approximately 0.187 ms will be broadened by the filter, establishing a lower limit on the observable peak widths. In our experiments, the majority of measured peak widths exceed this theoretical limit, validating that the 2 kHz filter setting provides sufficient temporal resolution for analyzing the dynamics of hydrogen adsorption and evolution on Pd NPs. It should be noted that the transient responses are not perfectly Gaussian; therefore, the true temporal resolution could be slightly better than 0.187 ms.

E Appendix E: Thermodynamic Limit of Hydrogen absorption in Pd Nanoparticles

The maximum hydrogen occupancy (x) in Pd NPs under electrochemical conditions can be estimated by balancing the chemical potential of absorbed hydrogen in the Pd lattice ($\mu_{\mathrm{H,Pd}}(x)$) with the electrochemical potential of solvated protons and electrons ($\mu_{\mathrm{H^+}} + \mu_{\mathrm{e^-}}$), as shown in Equation (21) and (22). Assuming $\mu^0_{\mathrm{H,Pd}} = 0$ for simplicity, the equilibrium condition becomes:

$$RT \ln\left(\frac{x}{1-x}\right) = RT \ln a_{\mathrm{H^+}} - eE_{\mathrm{RHE}}$$

As shown in **Appendix A**, $E_{\mathrm{RHE}} \approx -0.408$ V Then, calculate:

$$RT \ln a_{\mathrm{H^+}} = 8.314 \times 298 \times \ln(0.025) \times 0.001 = -9.1345 \text{ kJ/mol}$$

$$-eE_{\mathrm{RHE}} = -(-0.408) \times 96485/1000 = 39.39 \text{ kJ/mol}$$

$$RT \ln a_{\mathrm{H^+}} - eE_{\mathrm{RHE}} = -9.1345 + 39.39 = 30.2555 \text{ kJ/mol}$$

Thus:

$$\ln\left(\frac{x}{1-x}\right) = \frac{30.2555}{2.4786} \approx 12.21$$

Solving for x:

$$\frac{x}{1-x} = e^{12.21} \approx 2.01 \times 10^5$$

$$x = \frac{2.01 \times 10^5}{1 + 2.01 \times 10^5} \approx 0.999995$$

Therefore, the thermodynamic maximum hydrogen occupancy under the applied conditions is:

$$\boxed{x_{\mathrm{thermo}} \approx 1}$$

F Appendix F: Calculation of Hydrogen Fraction in Pd NPs After Collision

To estimate the hydrogen fraction (x) in Pd NPs following a collision event, we use Faraday's law:

$$Q = n_{\mathrm{H}} F$$

where: - $Q = 78.809$ fC $= 78.809 \times 10^{-15}$ C, - $F = 96485$ C mol^{-1}.

Thus:

$$n_{\mathrm{H}} = \frac{78.809 \times 10^{-15}}{96485} = 8.17 \times 10^{-19} \text{ mol}$$

The number of moles of Pd atoms per NP is:

$$n_{\mathrm{Pd}} = \frac{\rho_{\mathrm{Pd}} \times V_{\mathrm{NP}}}{M_{\mathrm{Pd}}}$$

where: - $\rho_{\mathrm{Pd}} = 12.0$ g cm^{-3}, - $M_{\mathrm{Pd}} = 106.42$ g mol^{-1}, - $V_{\mathrm{NP}} = \frac{4}{3}\pi r^3$, - $r = 28$ nm $= 2.8 \times 10^{-6}$ cm.

Calculating:

$$V_{\mathrm{NP}} = \frac{4}{3}\pi (2.8 \times 10^{-6})^3 = 9.198 \times 10^{-17} \text{ cm}^3$$

$$n_{\mathrm{Pd}} = \frac{12.0 \times 9.198 \times 10^{-17}}{106.42} = 1.037 \times 10^{-17} \text{ mol}$$

Therefore, the hydrogen occupancy fraction is:

$$x = \frac{n_{\mathrm{H}}}{n_{\mathrm{Pd}}} = \frac{8.17 \times 10^{-19}}{1.037 \times 10^{-17}} \approx 0.079$$

Thus, the hydrogen fraction in the Pd NPs after collision is approximately:

$$\boxed{x \approx 0.079}$$

G Appendix G: Determination of Steady-State Current

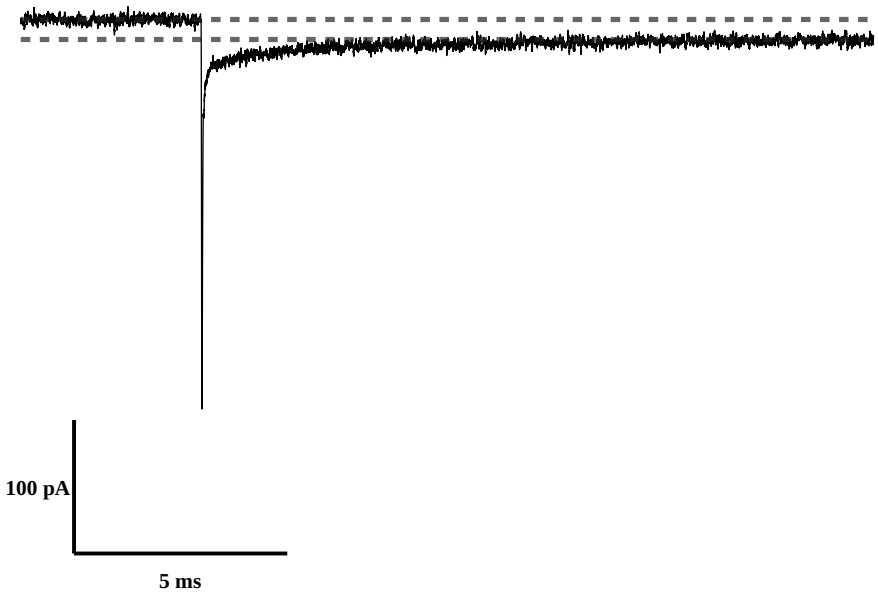

Figure S5: The quasi-steady state current was measured as the difference between the two grey dashed line. It can be observed that after the collision, it took the current to undergo some decay and return to the true baseline.

H Appendix H: Volmer Fitting on Steady-State Current

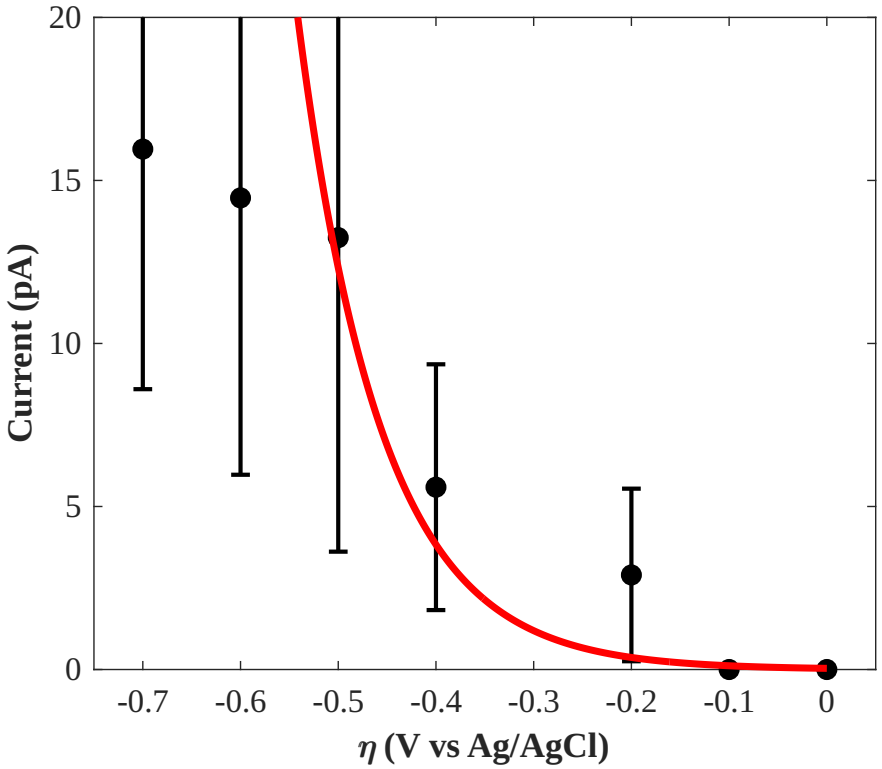

Figure S6: Quasi-steady state current fitting with Volmer step model (Equation 24).
Here, nonlinear least-squares fitting of our current–overpotential data using the Volmer-only model yielded a strongly negative coefficient of determination (R= -44.1) and an unrealistically low standard rate constant. ($k^0 = 7 \times 10^{-7}$m/s). Moreover, the optimization routine terminated without iterations, indicating that the model failed to meaningfully capture the data. The Volmer model drastically underestimated the current at moderate overpotentials and could not reproduce the observed nonlinear trend (Figure S6). These results confirm that the Volmer step is not the rate-limiting process under our conditions, and instead behaves as a fast, quasi-equilibrated adsorption step.

I Appendix I: Explanation of Wide Error Bar

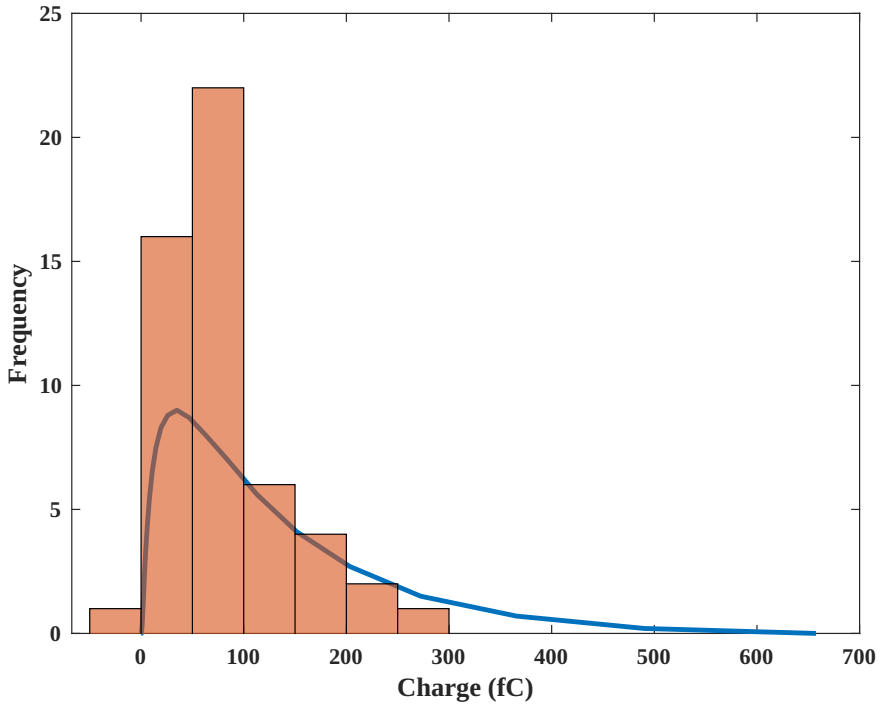

Figure S7: Comparison between the experimentally measured charge distribution from single-particle collisions (bars) and the theoretical distribution (line) derived from DLS data, assuming single-layer hydrogen adsorption where charge scales with particle surface area. The strong agreement between the two indicates that the broad spread in measured charges is primarily attributable to the intrinsic size distribution of the Pd NPs. The slight rightward shift of the histogram peak relative to the theoretical curve is likely due to partial hydrogen absorption occurring on the Pd surface at –0.7 V vs. Ag/AgCl in 25 mM perchloric acid.